

Phoretic self-propulsion at finite Péclet numbers

Sébastien Michelin^{1,*} and Eric Lauga^{2,†}

¹*LadHyX – Département de Mécanique, Ecole Polytechnique – CNRS, 91128 Palaiseau, France*

²*Department of Applied Mathematics and Theoretical Physics,
University of Cambridge, Cambridge CB3 0WA, United Kingdom*

(Dated: March 17, 2014)

Phoretic self-propulsion is a unique example of force- and torque-free motion on small scales. The classical framework describing the flow field around a particle swimming by self-diffusiophoresis neglects the advection of the solute field by the flow and assumes that the chemical interaction layer is thin compared to the particle size. In this paper we quantify and characterize the effect of solute advection on the phoretic swimming of a sphere. We first rigorously derive the regime of validity of the thin-interaction layer assumption at finite values of the Péclet number (Pe). Within this assumption, we solve computationally the flow around Janus phoretic particles and examine the impact of solute advection on propulsion and the flow created by the particle. We demonstrate that although advection always leads to a decrease of the swimming speed and flow stresslet at high values of the Péclet number, an increase can be obtained at intermediate values of Pe. This possible enhancement of swimming depends critically on the nature of the chemical interactions between the solute and the surface. We then derive an asymptotic analysis of the problem at small Pe allowing to rationalize our computational results. Our computational and theoretical analysis is accompanied by a parallel study of the role of reactive effects at the surface of the particle on swimming (Damköhler number).

I. INTRODUCTION

Self-propulsion at low Reynolds number is usually associated with the biological world. Indeed, many cellular organisms display some form of motility in fluids, in both prokaryotic and eukaryotic worlds [8]. Since the equations of motion are linear in this regime, the type of motion leading to self-propulsion have to be non-time-reversible [36]. This is typically achieved through the actuation of cellular appendages called flagella or cilia which act on a surrounding viscous fluid in a wave-like fashion [9, 25].

Beyond the biological world, artificial micro-scale swimmers have received increasing attention in recent years, motivated in part by their potential future use in a biomedical context [30]. The design of most synthetic swimmers to date has been inspired by that seen in the biological world, and have thus attempted to reproduce for example the two-dimensional beating of a sperm flagellum [13] or the three-dimensional rotation of a bacterial flagellum [16, 17, 47]. In all these cases, the actuation is not embedded in the swimmer itself or the surrounding fluid, but is due to the use of external fields, typically magnetic.

A promising alternative to design truly self-propelled swimmers takes advantage of the short-range interaction between the surface of a colloidal particle and an outer field gradient (e.g. solute concentration, temperature or electric field) to locally create fluid motion in the vicinity of a particle boundary [1]. These so-called phoretic mechanisms are responsible for the migration of isotropic particles in externally-imposed gradients. Furthermore, they may be exploited to generate self-propulsion when the particle is itself able to generate local gradients, for example through chemical reaction or heat radiation, an idea which has lead to significant activity in the physics and chemistry communities [11, 15, 18–22, 33]. Such swimmers are usually referred to as phoretic.

Physically, when the interaction layer (chemical, electrical, temperature...) is thin compared to the particle size, phoretic effects amount to generating a distribution of slip velocities at the particle surface [23], and can thus be thought of as a biomimetic analog to the propulsion by dense arrays of short beating cilia [6]. In order to induce non-trivial tangential chemical gradients and slip velocities, anisotropic properties of the particle surface are essential for small particles [18, 19] and isotropic particles cannot swim unless they are large enough for a symmetry-breaking instability involving advection of the surrounding chemical field to take place [29]. The main advantage of this type of swimmer design is the fact that they can swim in the absence of any external field and thus represent true force-free,

*Electronic address: sebastien.michelin@ladhyx.polytechnique.fr

†Electronic address: e.lauga@damtp.cam.ac.uk

torque-free self-propulsion [44]. The diffusiophoretic propulsion of such solid particles share many similarities with self-propelled Marangoni droplets, which swim as a result of self-generated gradients of reactive surfactants [38, 42, 46]

In this paper, we focus on the case of self-diffusiophoresis where the slip velocities are induced through the chemical interactions between a diffusive solute and a particle whose surface partly acts as a catalyst for a chemical reaction. A classical continuum framework has been recently proposed to study the dynamics of an isolated phoretic particle through the coupling of a Stokes flow problem to the diffusing and reacting dynamics of the solute [19]. This original framework was based on three main assumptions: (i) the diffuse layer where the solute-particle interaction takes place was assumed to be infinitely thin, so that the phoretic effect can be accounted for by a slip velocity at the surface of the particle; (ii) the advection of the solute was neglected, effectively decoupling the solute diffusion dynamics from the Stokes flow problem; (iii) on the catalyst portion of the particle surface, the chemistry was described by a fixed-rate absorption or release of the solute. In recent years, this framework has been used and extended to study a variety of properties of the self-propulsion of asymmetric colloidal particles including advective effects [11, 12, 23], the role of geometry [34], the impact of more complex surface chemistry [14], or of the non-zero thickness of the interaction layer [37, 39].

In the coupled fluid-chemical transport problem, neglecting the advection of the solute significantly simplifies the mathematical analysis since it effectively decouples the two problems. The solute concentration satisfies a diffusion equation which can be solved first, and its solution can then be exploited in the fluid problem to compute the swimming speed and the flow field. This assumption of zero solute Péclet number, Pe , is particularly adapted when the size of the particle is small enough, when the particle activity and/or mobility are weak (in some well-defined sense, which will be detailed below) or when the solute diffusivity is large. However, advective effects may become significant when the particle is not small compared to $a_c = D/\mathcal{U}$ with D the solute diffusivity and \mathcal{U} the characteristic phoretic velocity [23]. This is particularly relevant in the case of large proteins/molecules when D is very small. The catalytic autodegradation of hydrogen peroxyde by platinum Janus particles, and the resulting locomotion through gradients of oxygen, corresponds to a critical size $a_c \approx 10\text{--}100\mu\text{m}$ [14, 20]. Large Pe values can also be obtained at much smaller scales when the chemical species correspond to larger molecules [such as surfactants, 42]. When Pe is no longer negligible, advection of the solute has been shown to significantly impact the velocity of such particles [23, 24, 29]. Furthermore, the validity of the slip-velocity assumption in the presence of strong advective effects needs to be investigated. Solute advection at large values of Pe will lead to chemical boundary layers and not only can advection within the diffuse layer become significant but the diffuse layer thickness might no longer be negligible compared to the concentration boundary layer.

In addition, most self-diffusiophoresis studies consider either a fixed absorption release of solute at their surface [19, 23, 37] or a one-step absorption reaction where the solute flux is proportional to its local concentration [11]. The former approach can be seen as a particular case of the latter where the solute concentration is only weakly impacted by the reaction and remains mainly set by its far-field value, a limit particularly adapted to that of small particles. The importance of reactive effects, measured by the Damköhler number Da , must still be quantified. For large values of Da , solute diffusion is too slow to refresh the solute content of the fluid near the surface of the particle and phoretic effects may be reduced, potentially impacting self-propulsion.

The goal of the present paper is to quantify and characterize the effect of advection and reaction on phoretic self-propulsion. We first introduce the general continuum phoretic model for a spherical particle with arbitrary surface chemical properties. Asymptotic expansions are then exploited to analyze in detail the validity of the thin-interaction layer limit in the presence of advective and reactive effects. Using this assumption, a mathematical and computational framework is obtained for solving the phoretic problem at arbitrary values of Pe and Da for axisymmetric particles, in particular for Janus particles possessing one chemically-active cap while the rest of the particle surface is chemically inert [43]. We then use computations to analyze the impact of advection and reaction on the swimming velocity and the flow field induced by the particle motion. We show in particular that advective effects can increase the swimming speed of phoretic swimmers and amplify the flow they induce in the far field. We finally use analytical calculations at small Pe and Da numbers to rigorously calculate the sensitivity to both advection and reaction of arbitrary Janus particles, thereby explaining our computational results.

II. AUTOPHORETIC PROPULSION

The dynamics of an isolated solid particle of radius a are considered in a fluid of density ρ_f and dynamic viscosity η_f . A solute S dispersed in the fluid and characterized by its concentration, $C(\mathbf{x}, t)$, interacts with the particle's surface through a short range potential $\Phi(\mathbf{x}) = k_B T \phi(\mathbf{x})$ where λ is the range of the interaction potential (i.e. $|\Phi|/k_B T \ll 1$ if $|\mathbf{x}| - a \gg \lambda$, where the centre of the coordinate system is taken to be at the centre of the sphere). The solute is characterized by a far-field concentration C_∞ and may be released and/or absorbed at the surface through chemical reaction.

In the following, a general framework is presented that can account for two different types of surface chemistry [29]: a fixed-flux absorption/release characterized by an activity \mathcal{A} or a fixed-rate one-step chemical reaction $S \rightarrow P$ characterized by a reaction rate \mathcal{K} . In the latter case, although both reactant S and product P may interact with the surface, we will neglect for simplicity the interaction with P but what follows may easily be generalized to account for the chemical interaction of both species with the surface. The chemical properties of the particle surface are then characterized either by a distribution of activity or of reaction rate.

The solute S is assumed to diffuse with diffusivity D and to be advected by the fluid flow. In the following, it is assumed that the Reynolds number $\text{Re} = \rho_f U a / \eta_f$ is small enough for both fluid and solid inertia to be negligible. If furthermore the particle density is taken equal to that of the fluid, then the particle is force-free and torque-free.

Near the particle, the interaction between the solute in suspension and the particle surface induces a force $-\nabla\Phi$ on a given solute molecule. As a result, the force density applied on the fluid is $-C(\mathbf{x})\nabla\Phi$. In a reference frame attached to the centre of the particle, the equations of motion for the fluid flow simplify to Stokes' equations

$$\mathbf{0} = -\nabla p + \eta_f \nabla^2 \mathbf{u} - C \nabla \Phi, \quad \nabla \cdot \mathbf{u} = 0, \quad (1)$$

subject to the far-field condition and the no-slip boundary condition on the particle surface ($r = a$ with $r = |\mathbf{x}|$)

$$\mathbf{u}(r \rightarrow \infty) \sim -\mathbf{U} - \mathbf{\Omega} \times \mathbf{x}, \quad \mathbf{u}(r = a) = 0. \quad (2)$$

In Eq. (2), $\{\mathbf{U}, \mathbf{\Omega}\}$ are the unknown translation and rotation velocity of the rigid particle, respectively.

The advection-diffusion for the solute is governed by the following equation

$$\frac{\partial C}{\partial t} + \nabla \cdot \mathbf{j} = 0, \quad (3)$$

where the solute flux \mathbf{j} includes advection by the flow, diffusion, and transport by the interaction potential as

$$\mathbf{j} = C\mathbf{u} - D \left(\nabla C + \frac{C \nabla \Phi}{k_B T} \right). \quad (4)$$

The solute concentration must also satisfy the far-field condition,

$$C(r \rightarrow \infty) \sim C_\infty. \quad (5)$$

Finally, the chemical properties of the particle surface control the surface flux. Denoting \mathbf{x}^S a point on the surface of the particle, we have

$$D\mathbf{n} \cdot \left(\nabla C + \frac{C \nabla \Phi}{k_B T} \right) \Big|_{(|\mathbf{x}^S|=a)} = \begin{cases} -\mathcal{A}(\mathbf{x}^S) & \text{(fixed-flux);} \\ \mathcal{K}(\mathbf{x}^S)C & \text{(fixed-rate).} \end{cases} \quad (6)$$

In the fixed-flux case, a positive activity corresponds to an emission of solute while negative activity corresponds to absorption. The one-step chemical reaction with fixed rate always corresponds to an absorption and can hence be seen as a negative activity depending on the local concentration. Note that we assume the basic mechanism of absorption/desorption of the reactant/product on the surface catalyst to be fast enough that the solute concentration on the surface is at equilibrium with its immediate fluid environment at all times.

This set of equations for $\{C, \mathbf{u}, p\}$ and $(\mathbf{U}, \mathbf{\Omega})$ is closed by imposing the force- and torque-free conditions on the particle

$$\iint_{r=a} \boldsymbol{\sigma} \cdot \mathbf{n} dS + \iiint_{\Omega_f} C \nabla \Phi d\Omega = 0, \quad (7)$$

$$\iint_{r=a} \mathbf{x} \times (\boldsymbol{\sigma} \cdot \mathbf{n}) dS + \iiint_{\Omega_f} \mathbf{x} \times (C \nabla \Phi) d\Omega = 0. \quad (8)$$

In Eq. (7) the total force applied on the particle is the sum of the hydrodynamic force, with stress tensor $\boldsymbol{\sigma} = -p\mathbf{1} + \eta_f(\nabla\mathbf{u} + \nabla\mathbf{u}^T)$, and of the interaction forces with the solute in the entire fluid domain. Since the solute-surface interaction is short-ranged, this is approximately equivalent to imposing zero-hydrodynamic force and torque conditions on any surface outside the interaction layer, e.g. a sphere of radius $R \gtrsim \lambda + a$.

Both the fixed-rate and fixed-flux approaches can be combined into a single framework by solving for $c = C - C_\infty$ instead of C . The advection diffusion problem is now written as

$$\frac{\partial c}{\partial t} + \mathbf{u} \cdot \nabla c = D \nabla \cdot \left(\nabla c + \frac{(c + C_\infty) \nabla \Phi}{k_B T} \right), \quad (9)$$

$$c(r \rightarrow \infty) \rightarrow 0, \quad (10)$$

$$D \mathbf{n} \cdot \left(\nabla c + \frac{(c + C_\infty) \nabla \Phi}{k_B T} \right) = -\mathcal{A}^* + \mathcal{K} c \quad \text{for } |\mathbf{x}^S| = a. \quad (11)$$

The fixed-flux approach is obtained for $\mathcal{K} = 0$ and $\mathcal{A}^* = \mathcal{A}$, while in the fixed-rate approach $\mathcal{K} \neq 0$ and $\mathcal{A}^* = -\mathcal{K} C_\infty$.

The problem is non-dimensionalized using a as characteristic length. Since c is the concentration distribution relative to its far-field value, its characteristic variations scale with the normal gradients imposed at the surface by chemistry. A natural scale for c is therefore $[c] = \mathcal{A}a/D$ with \mathcal{A} the typical magnitude of the modified activity (either given by the magnitude of $\mathcal{A}(\mathbf{x}^S)$ or by $\mathcal{K}C_\infty$ with \mathcal{K} the magnitude of \mathcal{K}). A characteristic scale for the velocity \mathbf{u} is obtained from the dominant balance in the diffuse layer between viscous diffusion and solute-surface interactions and is chosen as $[U] = k_B T \lambda^2 [c] / \eta_f a$, from which the characteristic pressure is obtained as $k_B T [c] (\lambda/a)^2$ and characteristic time as $a/[U]$. The phoretic propulsion problem above now becomes in dimensionless form

$$\nabla^2 \mathbf{u} - \nabla p = \frac{(c + c_\infty) \nabla \phi}{\varepsilon^2}, \quad \nabla \cdot \mathbf{u} = 0, \quad (12)$$

$$\text{Pe} \left(\frac{\partial c}{\partial t} + \mathbf{u} \cdot \nabla c \right) = \nabla \cdot (\nabla c + (c + c_\infty) \nabla \phi), \quad (13)$$

$$c(r \rightarrow \infty) \rightarrow 0, \quad \mathbf{u}(r \rightarrow \infty) \sim -(\mathbf{U} + \mathbf{\Omega} \times \mathbf{x}), \quad (14)$$

$$\mathbf{u}|_{|\mathbf{x}^S|=1} = \mathbf{0}, \quad \mathbf{n} \cdot [\nabla c + (c + c_\infty) \nabla \phi]|_{|\mathbf{x}^S|=1} = k(\mathbf{x}^S) + \text{Da} k(\mathbf{x}^S) c. \quad (15)$$

and is characterized by four non-dimensional numbers:

$$\text{Pe} = \frac{k_B T \mathcal{A} \lambda^2 a}{\eta_f D^2}, \quad \text{Da} = \frac{\mathcal{K} a}{D}, \quad \varepsilon = \frac{\lambda}{a}, \quad c_\infty = \frac{D C_\infty}{\mathcal{A} a}. \quad (16)$$

Note that in (15), $k(\mathbf{x}^S)$ is defined as $-\mathcal{A}^*/\mathcal{A}$ for both the fixed-flux and fixed-rate problems. The Péclet number, Pe , is the ratio of diffusive to advective timescales, the Damköhler number, Da , is the ratio of diffusive to reactive timescales, ε is the dimensionless range of the interaction potential, and c_∞ is the ratio of the far-field concentration to the typical variations of concentrations around the particle. Note that the equations above are valid even when ε is not small. In the next section, we consider the classical thin-layer limit, $\varepsilon \ll 1$, for finite values of both Pe and Da .

III. THE THIN-INTERACTION LAYER LIMIT AND ITS LIMITATIONS

Most studies on self-diffusiophoresis focus on the $\varepsilon \ll 1$ limit of short-ranged potential, when the solute-particle interactions are restricted to a thin boundary layer around the particle [18, 19]. In this thin-interaction layer limit, all phoretic effects are bundled into two boundary conditions applied on the outer boundary of the interaction layer which is identical to the particle surface in the limit $\varepsilon \ll 1$, namely a slip velocity due to tangential solute gradients and a normal solute flux imposed by the chemistry at the particle surface. In this section, we revisit this limit of short-range potential $\varepsilon \ll 1$, in order to investigate the validity of that framework when neither advection (Pe) nor reaction (Da) can be neglected. Diffusiophoresis shares several fundamental properties and mechanisms with other phoretic phenomena [1], and it should be noted that the “thin interaction layer” analysis discussed below shares many similarities with the “thin Debye layer” limit considered in classical work on electrophoresis [31, 35]. Recently, Ref. [45] proposed a detailed analysis of the asymptotic regime in the case of electrophoresis of particles in externally-imposed electric fields.

The main result of this section is to show that the validity conditions for each of the boundary conditions above correspond to two distinct mathematical limits. First, in the limit $\varepsilon^2 \text{Pe} \ll 1$, the flow outside the interaction layer can be solved for taking into account a slip velocity \mathbf{u}^S at the boundary given by

$$\mathbf{u}^S = M(\mathbf{I} - \mathbf{n}\mathbf{n}) \cdot \nabla c, \quad (17)$$

with the local mobility M defined from the local interaction potential profile. If additionally we have $\varepsilon\text{Pe} \ll 1$ then advection within the interaction layer is negligible, and the solute advection-diffusion outside this interaction layer can be solved for independently from the interaction layer dynamics by applying on the outer boundary of this layer the flux condition imposed by the chemistry at the particle surface.

Since we have $\varepsilon \ll 1$, then in order for both results to be valid we need to be in the limit $\varepsilon\text{Pe} \ll 1$. In the rest of Section III we present the technical derivation of these two conditions and readers mostly interested in the particle dynamics may easily skip these derivations, retaining only the two conclusions above. Note that the derivations and results presented in this section are valid regardless of the surface properties of the spherical particle (activity and interaction potential). In particular, they are applicable to both axisymmetric and non-axisymmetric distributions. In the following, $\zeta = (\theta, \phi)$ generically stands for the two angular coordinates in spherical polar coordinates and is used to characterize this angular (and not necessarily axisymmetric) dependence of the particle's properties.

The derivations below follow the classical approach of matched asymptotic expansions [4], distinguishing between an outer solution, for which $r - 1 = O(1)$ and corresponding to the region where solute-particle interactions are negligible, and an inner solution, obtained for $\rho = (r - 1)/\varepsilon = O(1)$ in the interaction layer [7, 37, 39].

A. Outer solution

Expanding all outer fields in the form of regular expansion in ε , $f = f_0(r, \zeta) + \varepsilon f_1(r, \zeta) \dots$, and provided that $\phi_0 = \phi_1 = 0$, which is expected for all classical interaction potential decaying at least as fast as $1/(r - 1)^2$, the outer problem becomes at leading order

$$\nabla^2 \mathbf{u}_0 - \nabla p_0 = 0, \quad \nabla \cdot \mathbf{u}_0 = 0, \quad (18)$$

$$\text{Pe} \left(\frac{\partial c_0}{\partial t} + \mathbf{u}_0 \cdot \nabla c_0 \right) = \nabla^2 c_0, \quad (19)$$

$$c_0(r \rightarrow \infty) \rightarrow 0, \quad \mathbf{u}_0(r \rightarrow \infty) \sim -\mathbf{U}_0 - \boldsymbol{\Omega}_0 \times \mathbf{x}, \quad (20)$$

and is identical to other advection-diffusion problems in Stokes flow, such as the feeding of model ciliates [27, 28]. First-order corrections in ε (namely all f_1 quantities) satisfy the exact same equations. For both problems, the boundary conditions at $r = 1$ must be obtained through matching with the inner solution by expanding the different fields for $r - 1 \ll 1$ as

$$f(r, \zeta) = f_0(1, \zeta) + (r - 1) \frac{\partial f_0}{\partial r}(1, \zeta) + \varepsilon f_1(1, \zeta) + o((r - 1), \varepsilon). \quad (21)$$

B. Inner solution

We now focus on the inner problem for $\rho = (r - 1)/\varepsilon = O(1)$. Defining $\tilde{\phi}(\rho, \zeta) = \phi((r - 1)/\varepsilon, \zeta)$, we can write $\tilde{\phi}$ as a regular expansion in ε as

$$\tilde{\phi}(\rho, \zeta) = \tilde{\phi}_0(\rho, \zeta) + \varepsilon \tilde{\phi}_1(\rho, \zeta) \dots, \quad (22)$$

and the same expansion can be carried out for the inner concentration \tilde{c} , and all velocity components. Anticipating on the dominant balance in the momentum equations, the inner pressure is expanded as

$$\tilde{p}(r, \mu) = \frac{\tilde{p}_0}{\varepsilon^2} + \frac{\tilde{p}_1}{\varepsilon} + \tilde{p}_2 + \dots \quad (23)$$

Note that this difference of scaling between the inner and outer pressures impose that $\tilde{p}_i(r \rightarrow \infty) \rightarrow 0$ for $i = 0$ and 1.

We now substitute these expansions into Stokes equations, Eq. (12). Keeping only the first two dominant terms,

they can be rewritten as

$$\frac{\partial \tilde{u}_{r0}}{\partial \rho} + \varepsilon \left[\frac{\partial \tilde{u}_{r1}}{\partial \rho} + 2\tilde{u}_{r0} + \nabla \cdot \tilde{\mathbf{u}}_{\parallel 0} \right] = O(\varepsilon^2), \quad (24)$$

$$\frac{\partial \tilde{p}_0}{\partial \rho} + (c_\infty + \tilde{c}_0) \frac{\partial \tilde{\phi}_0}{\partial \rho} + \varepsilon \left[\frac{\partial \tilde{p}_1}{\partial \rho} + (c_\infty + \tilde{c}_0) \frac{\partial \tilde{\phi}_1}{\partial \rho} + \tilde{c}_1 \frac{\partial \tilde{\phi}_0}{\partial \rho} - \frac{\partial^2 \tilde{u}_{r0}}{\partial \rho^2} \right] = O(\varepsilon^2), \quad (25)$$

$$\begin{aligned} \frac{\partial^2 \tilde{\mathbf{u}}_{\parallel 0}}{\partial \rho^2} - \nabla_{\parallel} \tilde{p}_0 - (c_\infty + \tilde{c}_0) \nabla_{\parallel} \tilde{\phi}_0 + \varepsilon \left[\frac{\partial^2 \tilde{\mathbf{u}}_{\parallel 1}}{\partial \rho^2} + 2 \frac{\partial \tilde{\mathbf{u}}_{\parallel 0}}{\partial \rho} - \nabla_{\parallel} \tilde{p}_1 - \tilde{c}_1 \nabla_{\parallel} \tilde{\phi}_0 - (c_\infty + \tilde{c}_0) \nabla_{\parallel} \tilde{\phi}_1 \right. \\ \left. + \rho \nabla_{\parallel} \tilde{p}_0 + \rho (c_\infty + \tilde{c}_0) \nabla_{\parallel} \tilde{\phi}_0 \right] = O(\varepsilon^2), \end{aligned} \quad (26)$$

with $\mathbf{u}_{\parallel} = (\mathbf{I} - \mathbf{e}_r \mathbf{e}_r) \cdot \mathbf{u}$ and $\nabla_{\parallel} p = (\mathbf{I} - \mathbf{e}_r \mathbf{e}_r) \cdot \nabla p$. Similarly, the advection-diffusion problem for the inner concentration \tilde{c} can be rewritten as

$$\begin{aligned} \frac{\partial}{\partial \rho} \left(\frac{\partial \tilde{c}_0}{\partial \rho} + (c_\infty + \tilde{c}_0) \frac{\partial \phi_0}{\partial \rho} \right) + \varepsilon \left[\frac{\partial}{\partial \rho} \left(\frac{\partial \tilde{c}_1}{\partial \rho} + \tilde{c}_1 \frac{\partial \phi_0}{\partial \rho} + (c_\infty + \tilde{c}_0) \frac{\partial \phi_1}{\partial \rho} \right) + 2 \left(\frac{\partial \tilde{c}_0}{\partial \rho} + (c_\infty + \tilde{c}_0) \frac{\partial \tilde{\phi}_0}{\partial \rho} \right) \right] \\ = \varepsilon \text{Pe} \tilde{u}_{r0} \frac{\partial \tilde{c}_0}{\partial \rho} + \varepsilon^2 \text{Pe} \left(\tilde{u}_{r1} \frac{\partial \tilde{c}_0}{\partial \rho} + \tilde{\mathbf{u}}_{\parallel 0} \cdot \nabla_{\parallel} \tilde{c}_0 \right) + O(\varepsilon^2, \varepsilon^3 \text{Pe}), \end{aligned} \quad (27)$$

with boundary condition at the sphere surface, Eq. (15), becoming

$$\frac{\partial \tilde{c}_0}{\partial \rho} + (c_\infty + \tilde{c}_0) \frac{\partial \tilde{\phi}_0}{\partial \rho} + \varepsilon \left[\frac{\partial \tilde{c}_1}{\partial \rho} + (c_\infty + \tilde{c}_0) \frac{\partial \tilde{\phi}_1}{\partial \rho} + \tilde{c}_1 \frac{\partial \tilde{\phi}_0}{\partial \rho} \right] = \varepsilon k(\zeta)(1 + \text{Da} \tilde{c}_0) + O(\varepsilon^2), \quad (28)$$

at $\rho = 0$.

At leading order, mass conservation, Eq. (24), imposes that $\partial \tilde{u}_{r0} / \partial \rho = 0$. Together with the impermeability condition at the particle boundary, this shows that

$$\tilde{u}_{r0}(\rho, \zeta) = 0. \quad (29)$$

At leading order, momentum conservation in the radial and azimuthal directions, Eqs. (25)–(26), lead to,

$$\frac{\partial \tilde{p}_0}{\partial \rho} + (c_\infty + \tilde{c}_0) \frac{\partial \tilde{\phi}_0}{\partial \rho} = 0, \quad (30)$$

$$\frac{\partial^2 \tilde{\mathbf{u}}_{\parallel 0}}{\partial \rho^2} - \nabla_{\parallel} \tilde{p}_0 - (c_\infty + \tilde{c}_0) \nabla_{\parallel} \tilde{\phi}_0 = 0. \quad (31)$$

Provided that $\varepsilon^2 \text{Pe} \ll 1$, Eqs. (27) and (28) can be solved to leading order as

$$\tilde{c}_0(\rho, \zeta) = -c_\infty + \mathcal{C}_0(\zeta) e^{-\tilde{\phi}_0(\rho, \zeta)}. \quad (32)$$

Substitution of this result into Eq. (30) together with the decay condition of \tilde{p}_0 and $\tilde{\phi}_0$ for $\rho \gg 1$ leads to

$$\tilde{p}_0(\rho, \zeta) = \mathcal{C}_0(\zeta)(e^{-\tilde{\phi}_0(\rho, \zeta)} - 1). \quad (33)$$

Finally, substituting this result into Eq. (31), we obtain after integration and rearrangement,

$$\tilde{\mathbf{u}}_{\parallel 0}(\rho, \zeta) = -\nabla_{\parallel} \mathcal{C}_0 \left[\int_0^\infty R \left(e^{-\tilde{\phi}_0(R, \zeta)} - 1 \right) dR + \int_\rho^\infty (\rho - R) \left(e^{-\tilde{\phi}_0(R, \zeta)} - 1 \right) dR \right] + \beta \rho, \quad (34)$$

where $\mathcal{C}_0(\zeta)$ and $\beta(\zeta)$ are to be determined through matching with the outer solution.

C. Matching at leading order - Slip velocity

Matching the outer and inner solutions at leading order shows that $\beta = 0$ and provides the following relations

$$c_0(1, \zeta) = \mathcal{C}_0(\zeta) - c_\infty, \quad (35)$$

$$u_{r0}(1, \zeta) = 0, \quad (36)$$

$$\mathbf{u}_{\parallel 0} = M(\zeta) \nabla_{\parallel} \mathcal{C}_0. \quad (37)$$

with M , the mobility coefficient, given by

$$M(\zeta) = - \int_0^\infty \rho \left(e^{-\tilde{\phi}_0(\rho, \zeta)} - 1 \right) d\rho. \quad (38)$$

Combining Eqs. (36)–(37), we therefore establish that, provided $\varepsilon^2 \text{Pe} \ll 1$, the outer problem can be solved at leading order using a slip boundary condition

$$\mathbf{u} = M(\mathbf{I} - \mathbf{nn}) \cdot \nabla c \quad \text{at} \quad r = 1, \quad (39)$$

characterized by the mobility coefficient $M(\zeta)$ in Eq. (38) [1]. For locally attractive interactions ($\phi_0 < 0$), the mobility coefficient is negative and the slip velocity is oriented down-gradient, while for locally repulsive interactions ($\phi_0 > 0$) the slip velocity is oriented in the direction of the tangential solute gradient.

D. Validity of the flux condition

Since the flux boundary condition in Eq. (15) does not appear at leading order, the slip velocity result, Eq. (39), is not sufficient to close the outer system formed by Eqs. (18)–(20). In order to obtain the additional boundary condition on c_0 , it is necessary to carry out the expansion in the inner region to the next order [see also the work of 45, for a similar treatment in the case of electrophoresis]. Provided $\varepsilon \text{Pe} \ll 1$, the next order contribution to the advection-diffusion equation and boundary condition, Eqs. (27)–(28), leads to

$$\frac{\partial \tilde{c}_1}{\partial \rho} + \tilde{c}_1 \frac{\partial \tilde{\phi}_0}{\partial \rho} = -(c_\infty + \tilde{c}_0) \frac{\partial \tilde{\phi}_1}{\partial \rho} + k(\zeta) + \text{Da} k(\zeta) \tilde{c}_0. \quad (40)$$

After integration, we obtain

$$\tilde{c}_1(\rho, \zeta) = e^{-\tilde{\phi}_0(\rho, \zeta)} \left[\mathcal{C}_1(\zeta) + \rho k(\zeta) \left(1 + \text{Da} (\mathcal{C}_0(\zeta) - c_\infty) \right) + k(\zeta) (\text{Da} c_\infty - 1) \int_\rho^\infty \left(e^{\tilde{\phi}_0(R, \zeta)} - 1 \right) dR - \mathcal{C}_0(\zeta) \tilde{\phi}_1 \right]. \quad (41)$$

Using the previous equation and Eq. (32), in the limit $\rho \gg 1$ and $\varepsilon \ll 1$, we have

$$\tilde{c} = \mathcal{C}_0(\zeta) - c_\infty + \varepsilon \rho [k(\zeta) + \text{Da} k(\zeta) (\mathcal{C}_0 - c_\infty)] + \varepsilon \mathcal{C}_1(\mu) + o(\varepsilon, \varepsilon \rho). \quad (42)$$

Matching with the expansion of the outer solution c when $(r - 1) \ll 1$, Eq. (21), we obtain

$$\frac{\partial c_0}{\partial r}(1, \zeta) = k(\zeta) + \text{Da} k(\zeta) c_0(1, \zeta). \quad (43)$$

This equation simply states that the diffusive flux at the outer boundary of the interaction layer is equal to the diffusive flux at the particle surface. In this limit, advection is negligible in the interaction layer and the solute simply diffuses in the radial direction. This provides the missing boundary condition for (\mathbf{u}_0, c_0) and leads to an autonomous and well-posed set of equations.

This condition however breaks down when advection within the diffuse layer becomes important and $\varepsilon \text{Pe} = O(1)$, or equivalently when $k_B T A \lambda^3 / \eta_f D^2 = O(1)$. That condition does not depend on the size a of the phoretic particle, but only on the surface properties and diffusivity coefficients. Current experimental applications correspond to interaction layers of typical thickness $\lambda \lesssim 1 \text{ nm}$ [14, 20], so that $\varepsilon = O(10^{-5} - 10^{-3})$ for micrometric particles, and therefore advective effects within the interaction layer are indeed negligible, even for $\text{Pe} = O(1)$.

Note that even in the absence of advective effects in the outer region ($\text{Pe} = 0$), advective effects within the interaction layer may modify significantly the diffusive flux when the interaction potential is strong enough for the adsorption length to be comparable to the particle's size [2]. Such effects are implicitly neglected here: our choice for the scaling of the flow velocity within the interaction layer assumes that the adsorption length and interaction layer thickness are comparable.

To conclude, it is noteworthy that the validity conditions for the two approximations resulting from the thin diffuse layer framework, namely the slip velocity and the boundary flux of solute, are mathematically different at high Pe , namely $\varepsilon \ll \text{Pe}^{-1/2}$ for the slip velocity definition vs. $\varepsilon \ll \text{Pe}^{-1}$ for the boundary flux of solute.

IV. SELF-PROPULSION OF AUTOPHORETIC JANUS PARTICLES AT FINITE PÉCLET AND DAMKÖHLER NUMBERS

In Sections IV–VI, we present a model for the autophoretic self-propulsion of axisymmetric particles based on these approximations and investigate the effect of Pe on the self-propulsion properties of autophoretic particles. We assume that ε is sufficiently small such that the limit $\varepsilon Pe \ll 1$ allows us to consider intermediate and large values of Pe . In that limit, the solute-particle interactions are entirely accounted for through a slip velocity, Eq. (15), and a flux condition, Eq. (17), both valid at its outer limit ($r = 1^+$).

Focusing on steady-state propulsion, the resulting phoretic problem is expressed as

$$\nabla^2 \mathbf{u} - \nabla p = 0, \quad \nabla \cdot \mathbf{u} = 0, \quad (44)$$

$$Pe \mathbf{u} \cdot \nabla c = \nabla^2 c, \quad (45)$$

$$c \rightarrow 0 \quad \text{and} \quad \mathbf{u} \sim -(\mathbf{U} + \mathbf{\Omega} \times \mathbf{x}) \quad \text{for} \quad r \rightarrow \infty, \quad (46)$$

$$\frac{\partial c}{\partial r} = k(\zeta)(1 + Da c) \quad \text{and} \quad \mathbf{u} = M(\zeta)(\mathbf{I} - \mathbf{nn}) \cdot \nabla c \quad \text{for} \quad r = 1, \quad (47)$$

The swimming velocity and rotation rate are obtained using the reciprocal theorem for a force-free and torque-free particle [40] and given by

$$\mathbf{U} = -\frac{1}{4\pi} \int_{r=1} \mathbf{u}_{||} dS, \quad \mathbf{\Omega} = -\frac{3}{8\pi} \int_{r=1} \mathbf{n} \times \mathbf{u}_{||} dS. \quad (48)$$

The problem now depends only on two dimensionless parameters, Da and Pe . The Damköhler number characterizes the importance of diffusion in controlling the surface kinetics of the solute. When $Da = 0$, diffusion is fast enough for the absorption of solute to be controlled by its far-field concentration and to be essentially independent on the local fluctuations of solute concentration (fixed-flux framework). In contrast, for finite Da , the concentration fluctuations resulting from the absorption of solute at the interface are significant. The Péclet number, Pe , characterizes the relative importance of advection and diffusion on the solute distribution. When $Pe = 0$, the flow resulting from phoretic effects at the particle surface has no impact on the solute distribution. Both non-dimensional numbers can also be seen as a measure for the particle size and the classical framework ($Pe = Da = 0$) is therefore appropriate for small particles. Here, we thus investigate the advective and reactive effects when the particle size is no longer small enough for both Pe and Da to be neglected.

For simplicity, we exclusively focus on the absorption of a solute through chemical reaction ($k > 0$), and the “release” problem is easily obtained from our results by changing M into $-M$. We also assume in the main text that the mobility is uniform, i.e. that the interaction potential is isotropic around the sphere, $\phi(\mathbf{x}) = \phi(|\mathbf{x}|)$. However, as we show in Appendix A, our framework can also be used in the case of non-uniform mobility, and leads to a generalization of the results presented in the main text to arbitrary mobility distributions. Finally, we note that the magnitude of M effectively determines the characteristic velocity outside the diffuse layer. Therefore, it is more relevant to rescale the velocity (and pressure) so as to include the effect of the potential distribution. The characteristic velocity scale is now

$$[U] = \frac{k_B T \lambda^2 [c]}{\eta_f a} \left| \int_0^\infty \rho \left(e^{-\tilde{\phi}_0(\rho)} - 1 \right) d\rho \right|, \quad (49)$$

so that the non-dimensional mobility is simply $M = \pm 1$.

A. The axisymmetric phoretic problem

From Eq. (48), we see that a sufficient condition for the self-propulsion of a phoretic particle relies on its ability to generate a slip velocity field at its surface with a non-zero average. As the slip velocity originates from local solute gradients, one natural way to create self-propulsion is to consider non isotropic particles with a reactive cap on an otherwise-inert surface. Tangential gradients in solute concentrations are then expected to be generated between inert and active regions leading to slip velocity and locomotion. These so-called Janus particles are typically axisymmetric and have been the focus of most experimental, theoretical and numerical studies on autophoretic particles [11, 18, 19, 21, 23, 37].

For such axisymmetric particles, the chemical properties of the surface are characterized by an activity $k = k(\mu)$ where $\mu = \cos \theta$, with θ the polar angle with respect to the axis of symmetry \mathbf{e}_z in spherical polar coordinates. The

solute concentration and the flow field are also axisymmetric, and we denote $c = c(r, \mu)$, $\mathbf{u} = u_r(r, \mu)\mathbf{e}_r + u_\theta(r, \mu)\mathbf{e}_\theta$. Consequently the motion of the particle is a pure translation along \mathbf{e}_z , $\mathbf{U} = U\mathbf{e}_z$, with no rotation, $\boldsymbol{\Omega} = 0$.

In this setting, the Stokes flow problem can be solved explicitly using the squirmer formulation [6, 27]. The flow velocity is completely determined by the streamfunction ψ , obtained as the superposition of orthogonal modes

$$\psi(r, \mu) = \sum_{n=1}^{\infty} \frac{2n+1}{n(n+1)} \alpha_n \psi_n(r) (1 - \mu^2) L'_n(\mu), \quad (50)$$

where $L_n(\mu)$ is the n th Legendre polynomial and

$$\psi_1(r) = \frac{1-r^3}{3r}, \quad \psi_n(r) = \frac{1}{2} \left(\frac{1}{r^n} - \frac{1}{r^{n-2}} \right) \text{ for } n \geq 2. \quad (51)$$

The intensities of the squirring modes, α_n , are obtained through projection of the slip velocity $u_\theta(1, \mu)$ as

$$\alpha_n = \frac{1}{2} \int_{-1}^1 \sqrt{1-\mu^2} L'_n(\mu) u_\theta(1, \mu) d\mu. \quad (52)$$

The first squirring mode, α_1 , is the only one contributing to the swimming velocity of the particle, so that $\mathbf{U} = \alpha_1 \mathbf{e}_z$. The second squirring mode, α_2 , includes the slowest decaying contribution to the flow field, namely that of a symmetric force-dipole of intensity $\Sigma = 10\pi\alpha_2$. The contribution of this particle to the bulk stress takes the form of a stresslet $\boldsymbol{\Sigma} = \Sigma(\mathbf{pp} - \mathbf{I}/3)$ [3]. For $\Sigma > 0$ ($\alpha_2 > 0$), this flow field is equivalent to a so-called puller swimmer swimming flagella first (such as the alga *Chlamydomonas*), while $\Sigma < 0$ ($\alpha_2 < 0$) corresponds to a pusher swimming body first (such as most flagellated bacteria and spermatozoa).

With this formalism, the flow field is completely characterized and determined by the intensities of the squirring modes $\{\alpha_n\}_n$. Decomposing the surface reaction rate, $k(\mu)$, and solute distribution, $c(r, \mu)$, onto Legendre polynomials,

$$k(\mu) = \sum_{p=0}^{\infty} k_p L_p(\mu), \quad c(r, \mu) = \sum_{p=0}^{\infty} c_p(r) L_p(\mu), \quad (53)$$

we can then rewrite the phoretic problem, Eqs. (44)–(45), as a set of non-linearly coupled ODEs for the functions $c_p(r)$ ($p \geq 0$), from which the characteristics of the flow fields can be retrieved. Specifically we obtain

$$\frac{d}{dr} \left(r^2 \frac{dc_p}{dr} \right) - p(p+1)c_p = \text{Pe} \sum_{n=1}^{\infty} \sum_{m=0}^{\infty} \alpha_n \left[A_{mnp} \psi_n \frac{dc_m}{dr} + B_{mnp} \frac{d\psi_n}{dr} c_m \right], \quad (54)$$

$$c_p(\infty) = 0, \quad (55)$$

$$\frac{dc_p}{dr}(1) = k_p + \text{Da} \sum_{m=0}^{\infty} \sum_{n=0}^{\infty} \frac{A_{mnp} k_n}{2n+1} c_m(1), \quad (56)$$

$$\alpha_n = -\frac{n(n+1)M}{2n+1} c_n(1) \quad \text{for } n \geq 1, \quad (57)$$

where the third-order tensors A_{mnp} and B_{mnp} are defined from the Legendre polynomials as [27]

$$A_{mnp} = \frac{(2p+1)(2n+1)}{2} \int_{-1}^1 L_m(\mu) L_n(\mu) L_p(\mu) d\mu, \quad (58)$$

$$B_{mnp} = \frac{(2p+1)(2n+1)}{2n(n+1)} \int_{-1}^1 (1-\mu^2) L'_m(\mu) L'_n(\mu) L_p(\mu) d\mu. \quad (59)$$

B. Janus particles

The Janus particles considered here consist of a reactive cap at one pole of the sphere while the rest of the particle is inert. A variety of Janus particles are considered here and they differ by the ratio of their inert to active surface area (Fig. 1). The chemical activity distribution is given by $k(\mu) = 1_{\{\mu > \mu_c\}}$, where μ_c denotes the angular size of the active region ($-1 \leq \mu_c \leq 1$). We assume for simplicity that the phoretic mobility is uniform ($M = \pm 1$). That assumption however does not impact our main results, which may easily be generalized to Janus mobility distributions

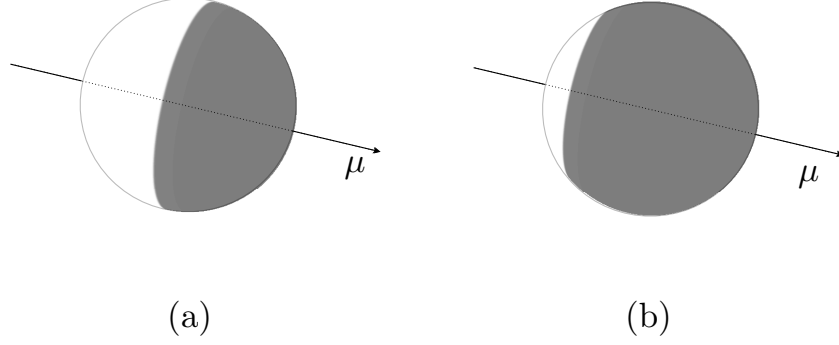


FIG. 1: Janus particles A and B considered in our computations: (a) Particle A is a hemispheric Janus particle with one half inert (white) and one half active (grey). (b) Particle B is a non-symmetric Janus swimmer with a large reactive pole (grey) and small inert area (white).

such that $M(\mu) = \pm k(\mu)$ as shown in Appendix A. For the choice $k(\mu) = 1_{\{\mu > \mu_c\}}$, the spectral coefficients k_n of the activity distribution can be obtained by projection of $k(\mu)$ onto the Legendre polynomials and we obtain

$$k_0 = \frac{1 - \mu_c}{2}, \text{ and } k_n = \frac{1}{2} [L_{n-1}(\mu_c) - L_{n+1}(\mu_c)] \text{ for } n \geq 1. \quad (60)$$

In the limit where both advective and reactive effects can be neglected ($\text{Pe} = \text{Da} = 0$), the diffusive problem for c , Eqs. (54)–(56), can be solved analytically along each azimuthal component and we obtain

$$c_p(r) = -\frac{k_p}{(p+1)r^{p+1}}. \quad (61)$$

Then, Eq. (57) provides the squirring mode intensities

$$\alpha_p = \frac{p k_p M}{2p+1}, \quad (62)$$

from which the entire flow field can be computed; in particular the reference swimming velocity and stresslet, thereafter referred to as U_0 and Σ_0 , are obtained as

$$U_0 = \frac{k_1 M}{3} = \frac{M}{4}(1 - \mu_c^2), \quad \Sigma_0 = 4\pi M k_2 = 5\pi M \mu_c(1 - \mu_c^2). \quad (63)$$

For our computations in Section V, we specifically focus on two such Janus particles denoted Particles A and B (Fig. 1) of uniform mobility $M = \pm 1$, this effectively amounting to four different configurations, or two pairs.

Particle A is a hemispheric (symmetric) Janus swimmer ($\mu_c = 0$) with one half chemically-active and the other half inert. The corresponding spectral coefficients k_n are computed as

$$k_0^A = \frac{1}{2}, \quad k_{2q}^A = 0, \text{ and } k_{2q-1}^A = (-1)^{q+1} \frac{4q-1}{4q-2} \frac{(2q)!}{[2^q q!]^2} \text{ for } q \geq 1. \quad (64)$$

In particular, $k_1^A = 3/4$ and $k_2^A = 0$, so that $U_0^A = M/4$ and $\Sigma_0^A = 0$. This is the particle with maximum swimming velocity in the limit where both advective and reactive effects are negligible ($\text{Pe} = \text{Da} = 0$). The sharpest concentration gradients are located near the equator for particle A, resulting in the largest slip velocities located on an extended surface and oriented mostly horizontally (as illustrated in Fig. 2a and c). In contrast, particle A has no stresslet in the $\text{Pe} = \text{Da} = 0$ limit and its far-field signature has a faster decay and is dominated by a source dipole and a force quadrupole.

Particle B is a non-symmetric Janus swimmer with $\mu_c = -1/\sqrt{3}$. It consists of a larger active cap and small inert portion. Using Eq. (60), one obtains that $k_1^B = 1/2$ and $k_2^B = 5/6\sqrt{3}$, so that for particle B, we get a smaller

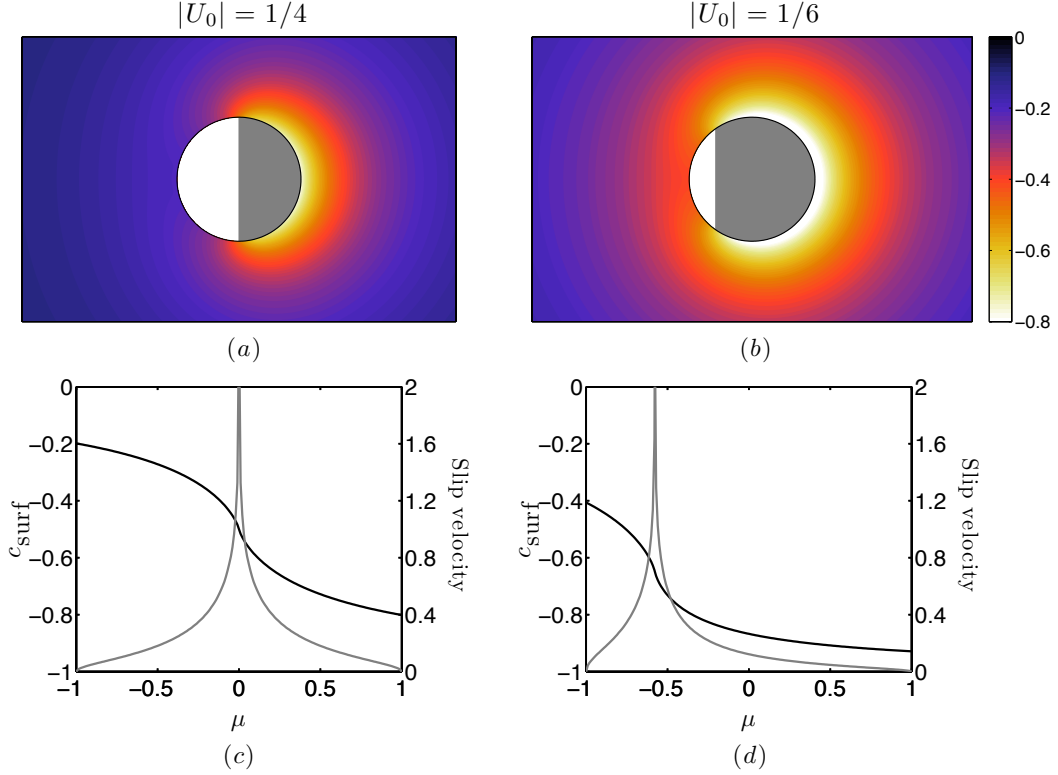


FIG. 2: (Colour online) Top: Relative solute concentration distribution, c , in the reference configuration with no advective or reactive effects ($\text{Pe} = \text{Da} = 0$) for (a) Janus particle A and (b) Janus particle B. The reactive cap is shown in grey and the inert portion in white. For $M = 1$ (resp. $M = -1$), the swimming velocity is oriented to the right (resp. left). Bottom: Surface solute concentration (black) and slip velocity (grey) along the surface in the case of positive mobility ($M = 1$) for (c) particle A and (d) particle B.

swimming velocity, $U_0^B = M/6$, and a finite stresslet, $\Sigma_0^B = -10\pi M/3\sqrt{3}$. The front between reactive and inert regions is located closer to the pole, and thus involves a smaller share of the particle surface creating slip velocities inclined away from the direction of motion and therefore a smaller swimming speed (see Fig. 2b and d). On the other hand, particle B corresponds to a maximum stresslet intensity for $\text{Pe} = \text{Da} = 0$, and as such is one of the Janus particle inducing the largest far-field hydrodynamic interactions with other particles.

Note that for both particles, the chemical reaction at the surface results in a reduction of the solute concentration near the reactive pole ($\mu = 1$). For a slip velocity oriented along (resp. against) the surface gradient, $M = 1$ (resp. $M = -1$), the slip velocity is oriented from the reactive to the inert pole (resp. from the inert pole to the reactive pole) resulting in a positive (resp. negative) swimming velocity.

C. Numerical solution

For finite values of Da and Pe , the phoretic problem, Eqs. (54)–(57), is solved numerically for each particle. The different azimuthal modes of the solute distribution, $c_p(r)$, are discretized on a stretched radial grid [27, 28], and an iterative process is followed:

- i. For an initial guess of the flow, determined by an initial guess of $\{\alpha_n^i\}_n$, the linear advection diffusion problem, Eqs. (54)–(56), is solved directly for $\{c_p(r)\}_p$ [27].
- ii. Using the solution of this advection-diffusion problem, Eq. (57) is used to obtain an updated estimate of the squirmer mode intensities, $\{\alpha_n^f\}_n$.
- iii. Broyden's method is used to solve iteratively the non-linear system $\mathbf{F}(\boldsymbol{\alpha}) = \boldsymbol{\alpha}^f - \boldsymbol{\alpha}^i$: knowing an estimate $\boldsymbol{\alpha}^n$

of the solution and an estimate of the inverse of the Jacobian matrix $\mathbf{J}_n^{-1} = [\nabla_{\alpha}\mathbf{F}(\alpha^n)]^{-1}$, a new estimate for both quantities is obtained as [10]

$$\alpha^{n+1} = \alpha^n - \mathbf{J}_n^{-1} \cdot \alpha^n, \quad (65)$$

$$\mathbf{J}_{n+1}^{-1} = \mathbf{J}_n^{-1} + \frac{(\Delta\alpha - \mathbf{J}_n^{-1}\Delta\mathbf{F}) \cdot (\Delta\alpha^T \cdot \mathbf{J}_n^{-1})}{\Delta\alpha^T \cdot \mathbf{J}_n^{-1} \cdot \Delta\alpha}, \quad (66)$$

where α^T is the transpose of the column vector α , $\Delta\alpha = \alpha^{n+1} - \alpha^n$, and $\Delta\mathbf{F} = \mathbf{F}(\alpha^{n+1}) - \mathbf{F}(\alpha^n)$. The iteration is initiated using either a previous computation or the reference solution ($\text{Da} = \text{Pe} = 0$), in which case the Jacobian matrix must be computed numerically for the initial step.

The number and position of the points on the radial grid, as well as the number of azimuthal modes used for the solute concentration distribution, are adjusted to the value of the Péclet number [26, 27]. Typical computations for moderate Pe include 120 azimuthal modes and 150 radial points. Truncation must also be introduced in the number of squirting modes used and the number of azimuthal components retained for $k(\mu)$. In the results presented below, typically $n_{\alpha} = 8$ squirting modes were used as well as $n_k = 12$ modes for the surface activity. These two parameters critically impact computational cost. Convergence tests performed showed that for Pe less than 100, the swimming velocity was only marginally impacted (less than 0.5%) when doubling n_{α} or n_k .

V. ADVECTIVE AND REACTIVE EFFECTS ON THE SELF-PROPULSION OF JANUS PARTICLES

Using the model and formalism presented in Section IV, we now investigate the effect of advection (Pe) and reaction (Da) on the self-propulsion of Janus phoretic particles. The asymmetry of the particles ensure that self-propulsion is achieved for all values of Pe and Da even in the purely diffusive regime $\text{Pe} = \text{Da} = 0$. Note that self-propulsion can also be achieved by isotropic or symmetric particles as an instability in the nonlinear advective coupling of solute dynamics to the phoretic flow around the particle [29]. In that case, and in certain conditions, a critical Pe exists above which symmetry-breaking leads to propulsion.

A. Advective effect for the fixed-flux limit ($\text{Da} = 0$)

We start by considering the effect of advection on phoretic locomotion. When Pe is increased, the solute concentration distribution around the particle is modified due to the advection of the solute by the flow resulting from the phoretic slip velocity. As a result, local concentration gradients and the slip velocity distribution are also impacted, and changes in the swimming velocity occur. For both Janus particles A and B, and for both values of the mobility ($M = \pm 1$), Figure 3 shows the dependence of the swimming velocity, U , and the stresslet intensity, Σ , on the Péclet number, Pe, in the absence of reactive effects ($\text{Da} = 0$). This situation corresponds therefore to a fixed-flux solute absorption at the surface. The case of a fixed-flux solute release is obtained directly by changing M into $-M$.

At large values of Pe, when advection dominates over solute diffusion, the magnitude of the swimming velocity is seen to always decrease for both particles. Analysis of the numerical data in Fig. 3 suggests that both $|U|, |\Sigma| \sim \text{Pe}^{-1/3}$ at large Pe. This scaling is consistent with that suggested by Ref. [23] and can be recovered from dimensional analysis as follows. At large Pe, the solute distribution resulting from the advection/diffusion problem is characterized by a boundary layer. The boundary layer thickness δ is the typical length scale associated with radial gradients of the solute concentration, while the typical length scale associated with tangential gradients remains $O(1)$ (i.e. the radius of the spherical particle). The boundary layer thickness δ is then obtained by balancing normal diffusive flux ($\sim \mathcal{C}/\delta^2$) with tangential advection ($\sim \text{Pe}\mathcal{U}\mathcal{C}$) near the surface, leading to $\delta \sim (\text{Pe}\mathcal{U})^{-1/2}$, with \mathcal{U} the typical slip velocity [27]. When $\text{Da} = 0$, the normal diffusive flux is fixed and $O(1)$, therefore $\mathcal{C} \sim \delta$ is the typical scale of variation of the solute concentration at the surface. Finally, the definition of the phoretic slip velocity in Eq. (17) imposes that $\mathcal{C} \sim \mathcal{U}$. Combining these three scaling arguments leads to $\mathcal{U}, \mathcal{C}, \delta \sim \text{Pe}^{-1/3}$, and the same dependence with Pe is recovered for the swimming velocity and stresslet intensity.

Although the autophoretic velocity decreases for all particles with the same scaling at large Pe, their finite-Pe evolutions strongly differ depending on the sign of the mobility. Particles A and B with positive mobility ($M = 1$) swim in the direction of their active pole (i.e. to the right in Figs. 1 and 2), and their velocity decreases monotonically in magnitude for all Pe. In contrast, particles with negative mobility ($M = -1$) swim toward their inert pole (i.e. to the left), and their velocity varies non-monotonically reaching a maximum magnitude around $\text{Pe} \approx 2$, before decreasing as $\text{Pe}^{-1/3}$. The existence of this velocity maximum is a new and notable result, which is not restricted to this type of swimmers. Indeed, several different particle activity distributions were tested, leading to the same result.

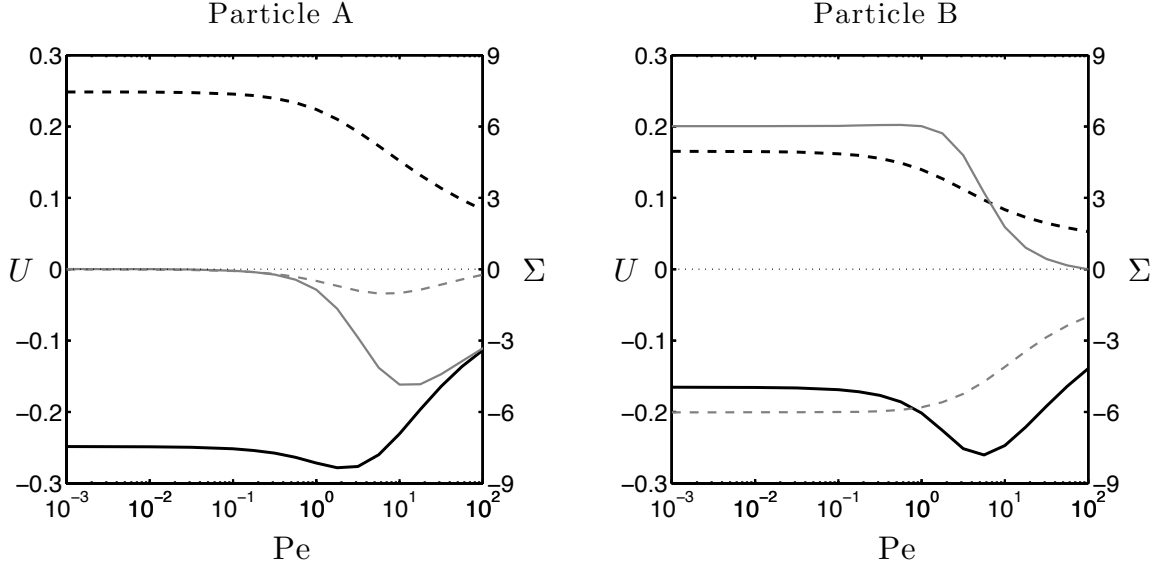


FIG. 3: Dependence of the swimming velocity (U , black) and stresslet magnitude (Σ , grey) on the value of Pe for particle A (left) and particle B (right) in the fixed-flux limit ($Da = 0$). For each case, results are shown for negative mobility $M = -1$ (solid) and positive mobility $M = 1$ (dashed).

For any given activity distribution $k(\mu)$, if the velocity magnitude of a particle of mobility M decreases monotonically with Pe , then for the particle with the same activity and opposite mobility $-M$, the velocity magnitude shows a peak in magnitude at intermediate values of Pe . For Janus particles, our simulations indicate in fact that regardless of the coverage of the active cap (i.e. for all μ_c), particles with negative mobility experienced a velocity peak at intermediate Pe , while particles with positive mobility exhibited a velocity decreasing monotonically with Pe .

For Janus particles, this difference in behaviour depending on the sign of the mobility can be qualitatively understood by comparing the solute concentration distribution around the particles (see Figs. 4 and 5) with the reference situation at $Pe = 0$ (Fig. 2). For all particles and all Pe , the chemical reaction near the active pole ($\mu = 1$) results in a depletion zone of the solute concentration in that region. When the particle swims toward the inert pole ($M = -1$, bottom plots in Fig. 4), advection of the fluid along the surface tends to concentrate this depleted region in a narrower region in the wake of the particle. Most importantly, advection brings in the vicinity of the front pole (here the inert one) fluid with higher solute content. Both effects exacerbate the concentration contrast between the fore and aft poles and the solute gradients along the surface, resulting in an increase in the slip and swimming velocity magnitudes when Pe is increased (Figs. 5 and 6). Note that the increase in slip velocity is limited to the reactive region. The slip velocity in the inert region remains roughly identical to the reference configuration. For absorbing particles with negative mobility (or equivalently for emitting particles with positive mobility), the advection of the solute by the phoretic flows introduces a positive feedback on the swimming velocity, that is similar to the one identified by Ref. [29] on isotropic particles and responsible, in that case, for symmetry breaking and propulsion. The similarity between these two problems is further discussed in Section VI.

In contrast, when the particle swims toward the reactive pole ($M = 1$, top plots in Fig. 4), the advection of richer fluid toward the reactive pole tends to increase the concentration in this depleted region, which is also spread on a larger part of the particle by the tangential advection along the surface. Both effects tend this time to reduce the concentration contrast between fore and aft poles resulting in a reduction of the slip and swimming velocity magnitudes (Fig. 6): solute advection by phoretic flows leads in this case to a negative feedback.

When $Pe \gg 1$, however, advection tends to homogenize the solute concentration near the boundary except in a narrow wake region: regardless of the sign of mobility and of the swimming direction, advective effects eventually penalize phoretic propulsion.

This difference of behaviour (i.e. existence of an extremum vs. monotonic decrease) is also observed for the stresslet, Σ , when $\Sigma_0 \neq 0$ (particle B). However, the magnitude of the peak differs only marginally from the stresslet amplitude in the reference configuration ($|(\Sigma_{\max} - \Sigma_0)/\Sigma_0| \approx 0.9\%$) so that it is barely visible on Figure 3. For Janus particle A, $\Sigma_0 = 0$ when $Pe = 0$ by symmetry, and the stresslet magnitude Σ is always negative for $Pe > 0$ and $Da = 0$. The impact of the phoretic particle on the far-field flow is that of a pusher swimmer, similar to that of most flagellated

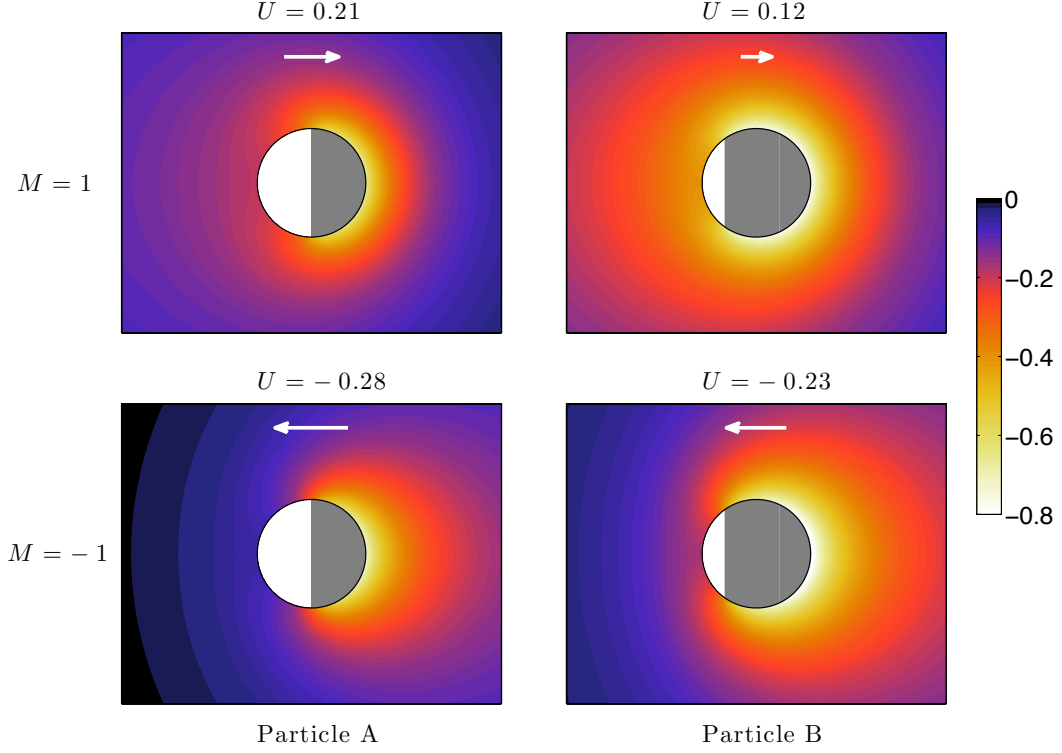


FIG. 4: (Colour online) Relative concentration distribution c around phoretic particle A (left) and particle B (right), for $Pe = 2$ and $Da = 0$. The swimming velocity of each particle is indicated by a white arrow. The reactive part of the surface is shown in grey.

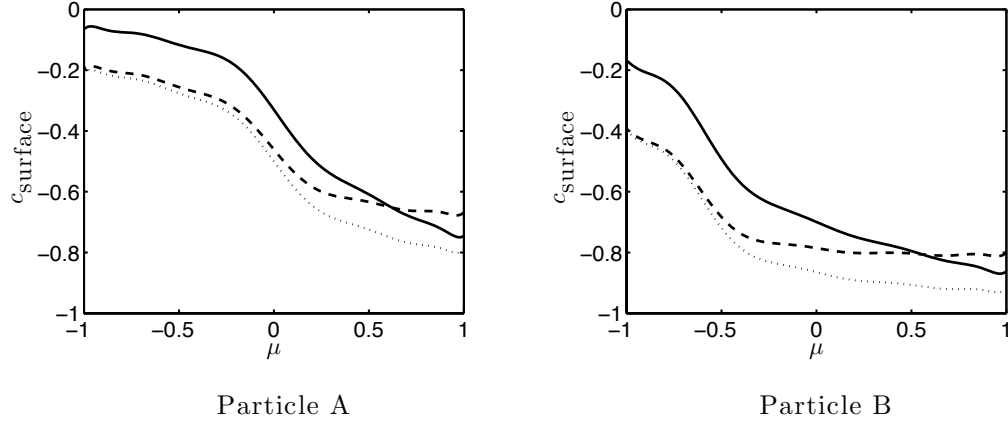


FIG. 5: Surface concentration distribution for particles A (left) and B (right) for $Pe = 2$ and $Da = 0$, in the case of positive mobility ($M = 1$, dashed) and negative mobility ($M = -1$, solid). The distribution in the reference configuration, $Pe = Da = 0$, is shown for reference as a dotted line.

bacteria. For both particles, the stresslet magnitude is maximum for $Pe = O(10)$. These results are confirmed and extended to arbitrary Janus particles in Section VI.

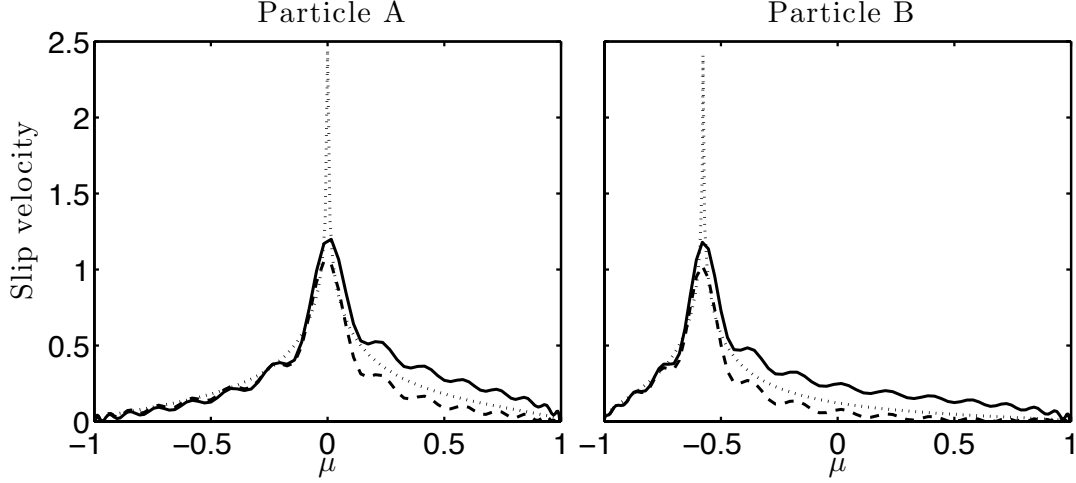


FIG. 6: Surface slip velocity distribution for particles A (left) and B (right) for $Pe = 2$ and $Da = 0$, in the case of positive mobility ($M = 1$, dashed) and negative mobility ($M = -1$, solid). The slip velocity in the reference configuration, $Pe = Da = 0$, is reported for reference as a dotted line. Note that due to the computational cost, only 32 modes were used to describe the slip velocity for $Pe = 2$ while the slip velocity in the reference configuration can be obtained analytically from Eqs. (61)–(62).

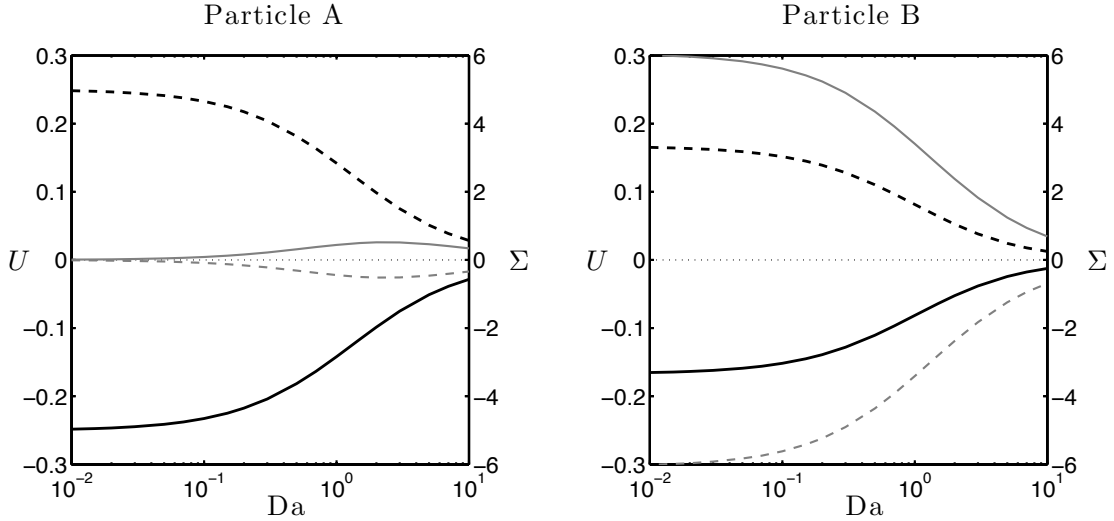


FIG. 7: Dependence of the swimming velocity (U , black) and stresslet magnitude (Σ , grey) with Da for particle A (left) and particle B (right) in the diffusive limit ($Pe = 0$). Results are obtained for both negative mobility $M = -1$ (solid) and positive mobility $M = 1$ (dashed).

B. Reactive effects in the diffusive limit ($Pe = 0$)

We now consider the effect of reaction kinetics on the swimming velocity when advective effects are neglected ($Pe = 0$). At finite values of Da , the rate of solute absorption becomes dependent on the local solute concentration. The reaction at the surface is fast enough for diffusion to be unable to maintain a relatively homogeneous background concentration of solute around the particles. In other words, the concentration changes induced by surface reaction are now of similar magnitude to the background/far-field concentration. As a result, the reaction rate will be reduced in regions where the solute concentration is lower, in particular near the active pole.

The dependence of the velocity and stresslet intensity with Da is shown on Fig. 7. In contrast with the evolution

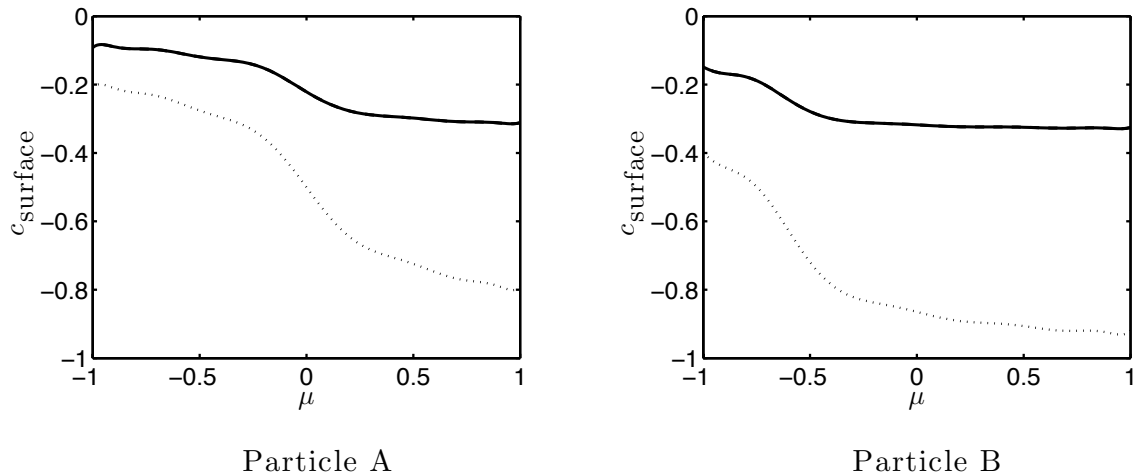


FIG. 8: Surface concentration distribution for particles A (left) and B (right) for $Da = 2$ and $Pe = 0$ (solid). Because advective effects are neglected, the concentration distribution is the same for both $M = 1$ and $M = -1$. The distribution in the reference configuration, $Pe = Da = 0$, is shown for reference as a dotted line.

of those quantities with solute advection, we observe a strong symmetry between the cases of positive and negative mobility: in the absence of any advective effects, solute concentration is determined purely by diffusion and has the same distribution regardless of the mobility of the particle. Particles of opposite mobilities have exactly opposite slip velocity distributions. Also, no peak in the velocity magnitude can be observed. Instead, the swimming velocity monotonically decreases with Da and tends to zero in the limit $Da \gg 1$. This is consistent with the comment above on the role of diffusion vs. reaction. Indeed, for larger values of Da , the reaction leading to the absorption of the solute is slowed down near the active pole (where the solute concentration is lowest), as illustrated in Fig. 8. As a result the tangential concentration gradients are reduced and so are the slip and swimming velocities, regardless of the value of the mobility M . In the limit of $Da \gg 1$, a decrease of the swimming velocity as Da^{-1} is observed. In that limit, the diffusion timescale is infinite, leading to a complete depletion of the most reactive regions. The perturbations to the solute concentration on the surface of the particle scale thus as $c \sim -Da^{-1}$, resulting in a similar scaling for the slip and swimming velocities.

C. Finite Péclet and Damköhler numbers

We show in Fig. 9 the dependence of both U and Σ with finite values of Pe and Da , and confirm the results obtained in the limits $Pe = 0$ and $Da = 0$. Regardless of the value of the Péclet number, the swimming velocity magnitude is observed to monotonically decrease with Da . Further, regardless of the value of the Damköhler number, the dependence of the swimming velocity with Pe is different for particles with positive and negative mobility. The swimming velocity of particles with positive mobility decreases monotonically while that of particles with negative mobility shows a maximum value for an intermediate Pe . Note also that the optimal Pe leading to this velocity maximum appears to be an increasing function of Da .

VI. SENSITIVITY OF ARBITRARY JANUS PARTICLES TO ADVECTIVE AND REACTIVE EFFECTS

In the previous section, the effects of advection (Pe) and reaction (Da) on the swimming velocity and stresslet intensity of two particular Janus particles were investigated computationally. In particular, it was shown that (i) advection may increase the magnitude of the self-propulsion, when the particle is swimming toward its inert pole at $Pe = 0$, (ii) reactive effects ($Da > 0$) always penalize self-propulsion and (iii) advective effects create a negative stresslet on particle A (for which $\Sigma_0 = 0$), resulting in a pusher swimmer. In this section, we first confirm these results and extend them to more general surface coverage using asymptotic analysis in the limit $(Pe, Da) \ll 1$. In particular, the sensitivity of the swimming velocity and stresslet to advective and reactive effects are mathematically determined

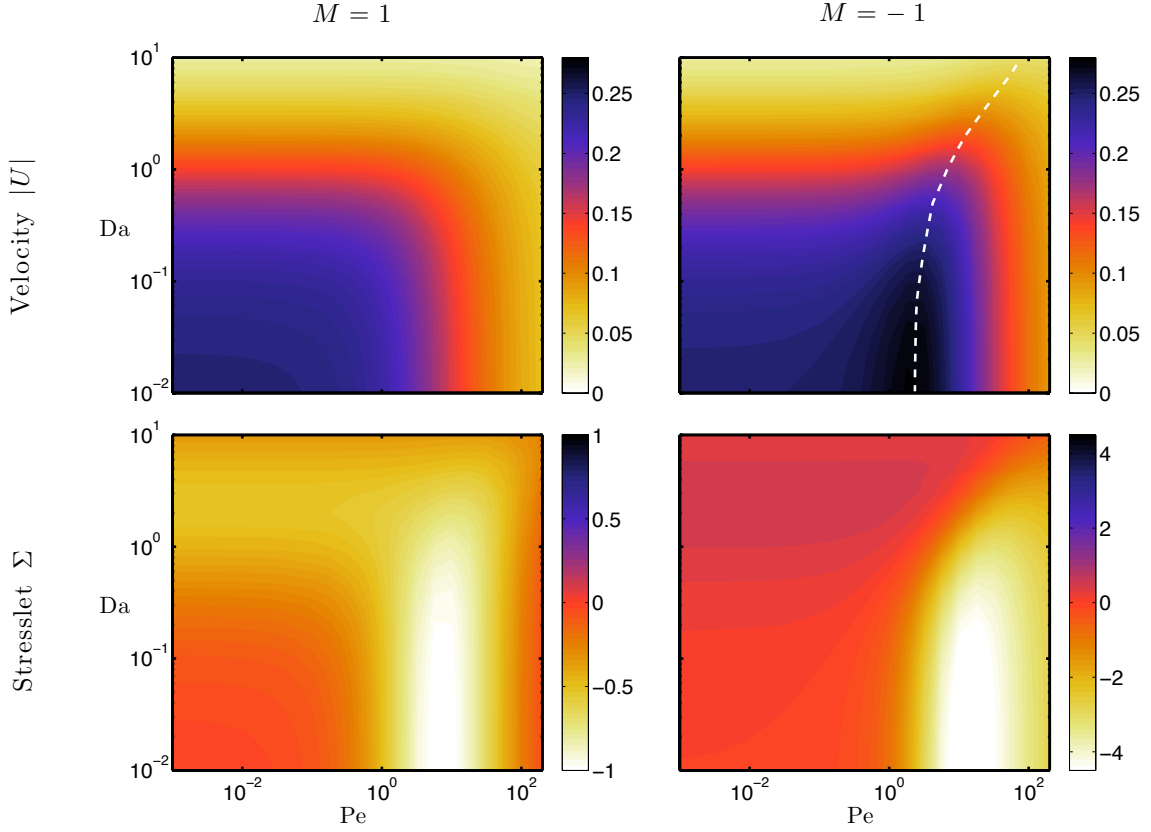


FIG. 9: (Colour online) Dependence of the magnitude of the propulsion velocity ($|U|$, top) and the stresslet intensity (Σ , bottom) with Pe and Da for the Janus particle A with $M = 1$ (left) or $M = -1$ (right). The white dashed line on the top-right figure indicates the evolution with Da of the optimal Pe for which the velocity magnitude is maximum at fixed Da .

by analytical calculations of four partial derivatives. For arbitrary Pe , the evolution of the swimming velocity and stresslet intensity for arbitrary Janus particles is then addressed numerically.

A. Asymptotic analysis for the autophoretic velocity

From Eqs. (54)–(57), we note that advective effects (Pe) and reactive effects (Da) are responsible for the coupling of the different azimuthal modes. In the limit where $Da = Pe = 0$, the different modes decouple and the solution is obtained explicitly as

$$\bar{c}_p(r) = -\frac{k_p}{(p+1)r^{p+1}}, \quad \bar{\alpha}_p = \frac{pk_p M}{2p+1}. \quad (67)$$

Defining the corrections $c'_p = c_p - \bar{c}_p$ and $\alpha'_p = \alpha_p - \bar{\alpha}_p$ to this reference solution, using

$$A_{mn1} = \frac{3(n+1)}{2n+3}\delta_{m,n+1} + \frac{3n}{2n-1}\delta_{m,n-1}, \quad (68)$$

$$B_{mn1} = \frac{3(n+2)}{2n+3}\delta_{m,n+1} + \frac{3(n-1)}{2n-1}\delta_{m,n-1}, \quad (69)$$

and keeping only the linear terms in the correction quantities, Eqs. (54)–(56) become for the swimming mode ($p = 1$)

$$\begin{aligned} \frac{d}{dr} \left(r^2 \frac{dc'_1}{dr} \right) - 2c'_1 = \text{Pe} \bar{\alpha}_1 \left[k_0 \left(\frac{1}{r^3} - 1 \right) + \frac{3k_2}{5r^5} \right] \\ + \frac{3\text{Pe}}{2} \sum_{n=2}^{\infty} \bar{\alpha}_n \left[k_{n+1} \left(\frac{2n+1}{(2n+3)r^{2n+3}} - \frac{2n-1}{(2n+3)r^{2n+1}} \right) \right. \\ \left. + k_{n-1} \left(\frac{1}{r^{2n+1}} - \frac{2n^2-3n+2}{n(2n-1)r^{2n-1}} \right) \right], \end{aligned} \quad (70)$$

$$c'_1(\infty) = 0, \quad (71)$$

$$\frac{dc'_1}{dr}(1) = -\text{Da} \sum_{n=0}^{\infty} \frac{3k_n k_{n+1}}{(2n+1)(n+2)}. \quad (72)$$

Using Eq. (67) and solving for $c'_1(r)$, we finally obtain as an expansion at small Pe and Da

$$U = \frac{k_1 M}{3} + \text{Pe} M^2 H_1 + \text{Da} M H_2 + o(\text{Da}, \text{Pe}), \quad (73)$$

where H_1 and H_2 are two constants that depend solely on the details of the surface activity distribution $k(\mu)$ as

$$H_1 = -\frac{k_1 k_0}{12} + \frac{k_1 k_2}{90} + \sum_{n=2}^{\infty} \frac{(4n-1)k_n k_{n+1}}{(2n+1)(2n+2)(2n+3)(2n+4)}, \quad (74)$$

$$H_2 = -\sum_{n=0}^{\infty} \frac{k_n k_{n+1}}{(n+2)(2n+1)}. \quad (75)$$

Specifically, the sensitivity of the velocity to reactive (Pe) and advective (Da) effects is obtained as

$$\left(\frac{1}{U} \frac{\partial U}{\partial \text{Pe}} \right)_{(\text{Pe}, \text{Da})=(0,0)} = \frac{3MH_1}{k_1}, \quad \left(\frac{1}{U} \frac{\partial U}{\partial \text{Da}} \right)_{(\text{Pe}, \text{Da})=(0,0)} = \frac{3H_2}{k_1} \quad (76)$$

and $k_1 > 0$ by convention for all Janus particles considered (reactive cap on the right).

This asymptotic prediction shows an excellent agreement with the results obtained in Section V for particles A and B (see Figure 10). For an arbitrary Janus particle, $k(\mu) = 1_{[\mu_c, 1]}$, the evolution of H_1 and H_2 with the size of the reactive cap (measured by $-1 \leq \mu_c \leq 1$) is shown in Fig. 11. For all Janus particles, H_1 and H_2 are always negative, but their dependence is non-symmetric with respect to $\mu_c = 0$ and two particles with reverse surface activity do not have the same sensitivity.

Since $H_2 < 0$ for all Janus particles, reactive effects always tend to reduce the velocity magnitude regardless of the sign of the mobility. This confirms our numerical observations in the previous section for particles A and B, and can actually be extended easily to any particle with a reactive “stripe” rather than a reactive “cap” (i.e. $k(\mu) = 1_{[\mu_c, \mu_u]}$). Reactive effects systematically reduce the solute consumption rate near the active surfaces, effectively penalizing the chemical activity of that region by limiting the supply in fresh solute.

In contrast, Eq. (76) shows that the sensitivity of the autophoretic velocity to advective effects depends on the sign of the mobility M . For all Janus particles, regardless of the size μ_c of the active region, a positive (resp. negative) mobility leads to a reduction (resp. increase) in their velocity magnitude from advective effects. This extends to arbitrary μ_c our numerical results for particles A and B. When the particle swims toward its reactive pole ($M > 0$), solute advection brings fluid of higher solute content closer to the reactive cap, reducing the contrast with the inert cap and the slip velocity magnitude. Instead, when the particle swims toward its inert pole ($M < 0$), advective effects increase the solute content near the front cap (the inert one) and concentrates the depleted region near the reactive pole, increasing the tangential solute gradients and the slip velocity.

B. Asymptotic analysis for the stresslet

Following a similar approach for the stresslet and linearizing Eqs. (54)–(56) for the $p = 2$ mode, one obtains the asymptotic result

$$\Sigma = 4\pi M k_2 + \text{Pe} M^2 \tilde{H}_1 + \text{Da} M \tilde{H}_2 + o(\text{Da}, \text{Pe}), \quad (77)$$

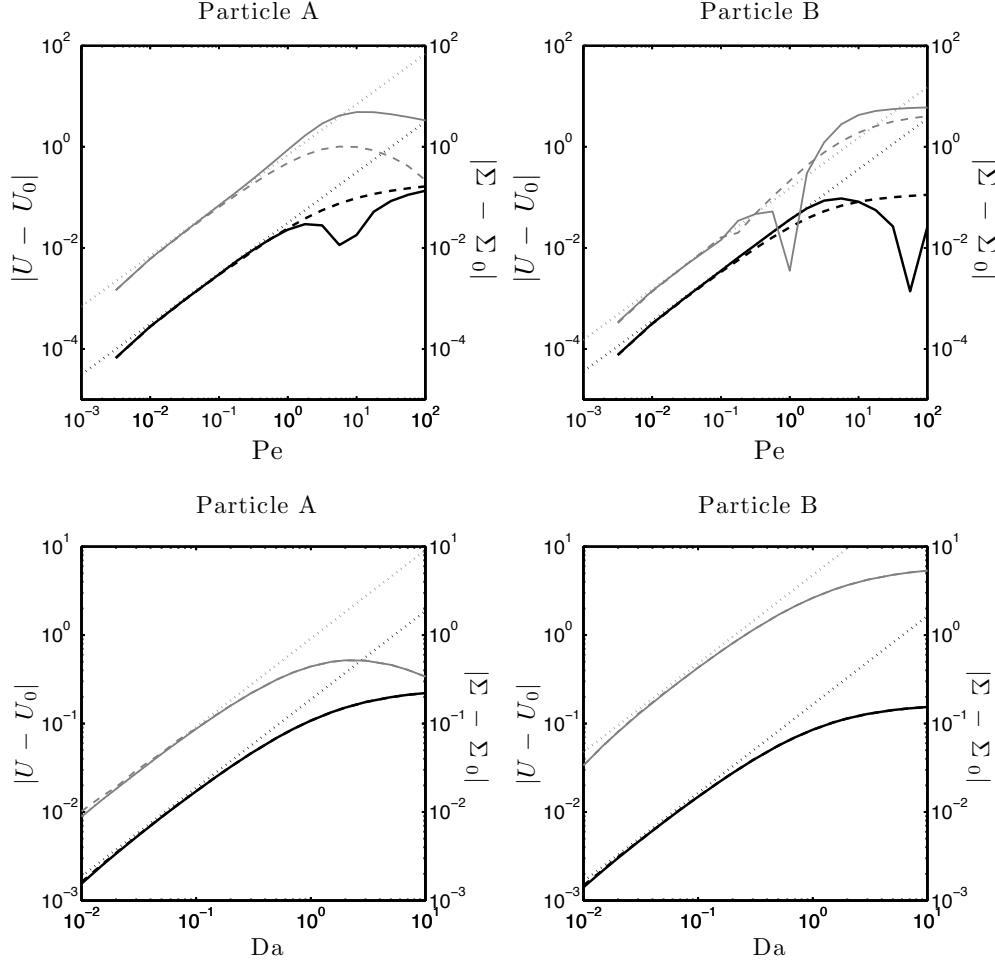


FIG. 10: Comparison between the numerical results of Section V with the asymptotic predictions for $Pe, Da \ll 1$ for particle A (left) and B (right): (Top) Evolution of $|U - U_0|$ (black) and $|\Sigma - \Sigma_0|$ (grey) with Pe for $Da = 0$, with U_0 and Σ_0 the phoretic velocity and stresslet intensity in the absence of advective or reactive effects; (Bottom) Evolution of the same quantities with Da for $Pe = 0$. For all figures, solid (resp. dashed) lines correspond to particles with negative (resp. positive) mobility. The dotted lines correspond to the predictions of Eqs. (73) and (77).

with

$$\tilde{H}_1 = 10\pi \left[-\frac{k_1^2 + k_0 k_2}{30} + \frac{k_1 k_3}{112} + \sum_{n=2}^{\infty} \left(\frac{3n(n-2)k_n^2}{2(n+1)^2(2n-1)(2n+1)(2n+3)} + \frac{3(3n-1)k_n k_{n+2}}{2(n+3)(2n+1)(2n+3)(2n+5)} \right) \right], \quad (78)$$

$$\tilde{H}_2 = -4\pi \sum_{n=0}^{\infty} \left[\frac{5n k_n^2}{(2n-1)(2n+1)(2n+3)} + \frac{15(n+2)^2 k_n k_{n+2}}{(2n+1)(2n+3)(2n+5)(n+3)} \right]. \quad (79)$$

This asymptotic result is, once again, in excellent agreement with the numerical results of Section V (Figure 10). These results also emphasize the difference in the evolution of the stresslet for particles A and B. For particle A, $k_2 = 0$ and $\Sigma_0 = 0$, and the asymptotic form in Eq. (77) is consistent with the stresslet at finite Pe (and $Da = 0$) being negative regardless of the sign of the mobility (Fig. 3). When $Da \neq 0$, Eq. (77) also confirms that particles A of opposite mobility have stresslets of different sign (see Fig. 7).

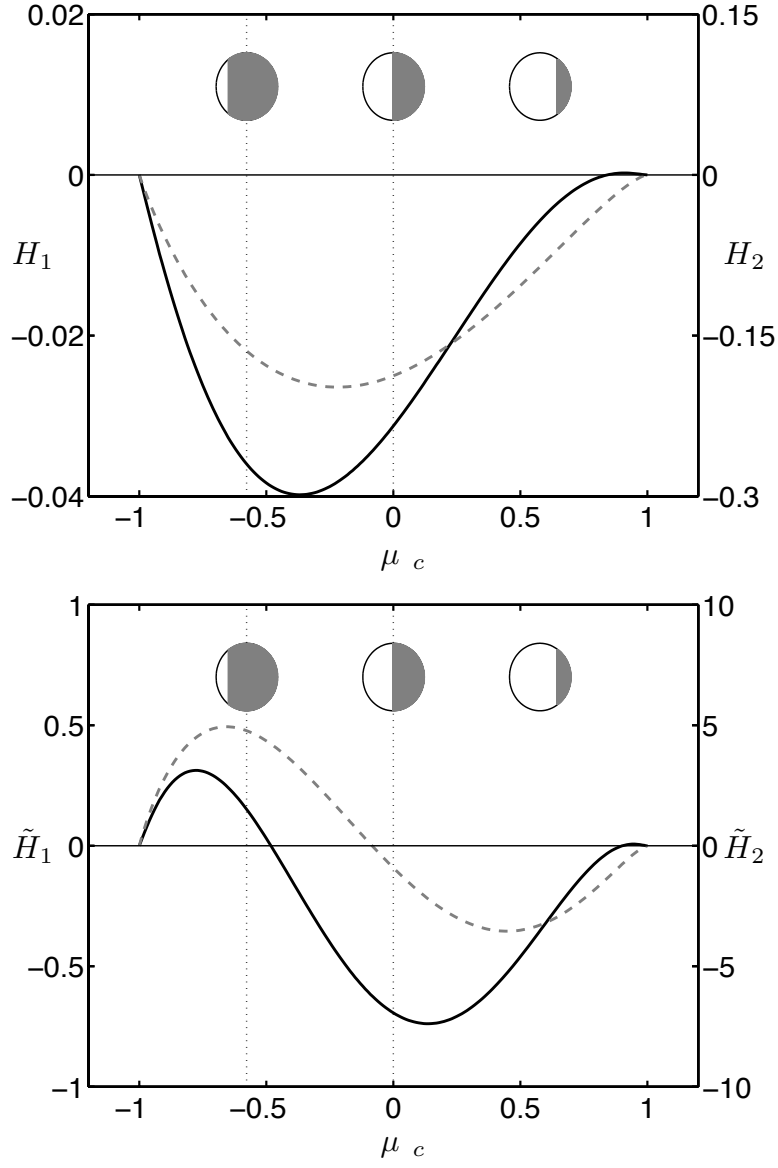


FIG. 11: Top: Dependence of the sensitivities H_1 (solid) and H_2 (dashed) of the swimming velocity magnitude with Pe and Da for a Janus particle with $k(\mu) = 1_{[\mu_c, 1]}$ and positive mobility. Bottom: Evolution of the sensitivities \tilde{H}_1 (solid) and \tilde{H}_2 (dashed) of the stresslet intensity with Pe and Da for the same particles. Particles A and B are shown by dotted lines.

When $\Sigma_0 \neq 0$ (e.g. particle B in Section V), the relative sensitivity of the stresslet is obtained as

$$\left(\frac{1}{\Sigma} \frac{\partial \Sigma}{\partial \text{Pe}} \right)_{(\text{Pe}, \text{Da})=(0,0)} = \frac{M \tilde{H}_1}{4\pi k_2}, \quad \left(\frac{1}{\Sigma} \frac{\partial \Sigma}{\partial \text{Da}} \right)_{(\text{Pe}, \text{Da})=(0,0)} = \frac{\tilde{H}_2}{4\pi k_2}. \quad (80)$$

For generic Janus particles that have a finite stresslet in the reference configuration ($\text{Pe} = \text{Da} = 0$), Eq. (80) shows that increasing reactive effects (Da) will have the same effect on particles of opposite mobility, while increasing advective effects will either lead to a maximum stresslet at intermediate Pe or a monotonic decrease of Σ with Pe , consistently with Figs. 3 and 7 (note that the maximum in Σ for particle B is of very small amplitude).

Finally, it should be noted that the results of the asymptotic analysis in Eqs. (73)–(75) and (77)–(79) are not restricted to Janus activity distributions but hold for any axisymmetric distribution of activity and could be used directly to investigate the sensitivity of a more general class of phoretic particles.

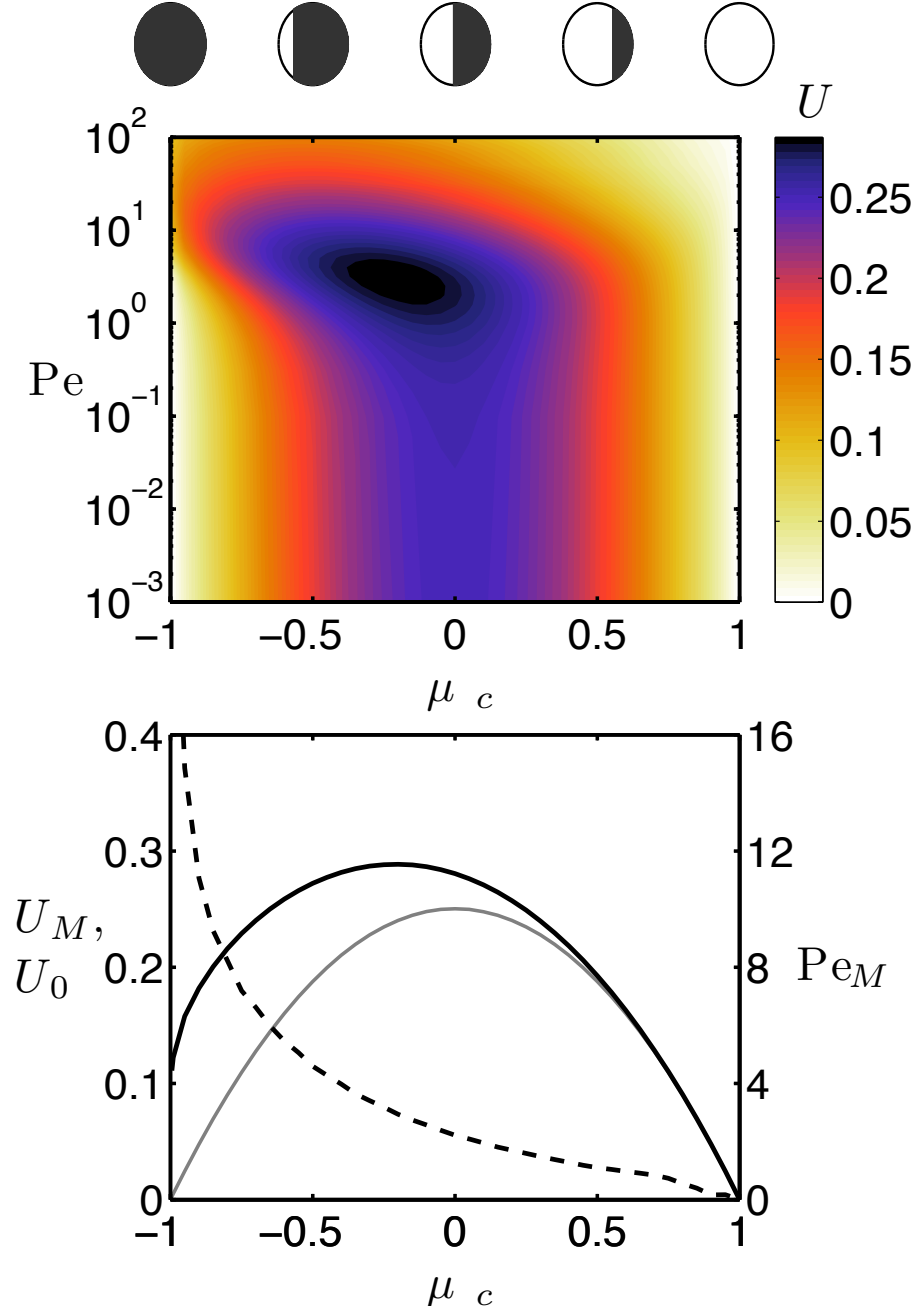


FIG. 12: (Colour online) Top: Dependence of the phoretic velocity magnitude on Pe and the relative size of the reactive cap μ_c (see illustration on top); $\mu_c = -1$ corresponds to a fully reactive particle and $\mu_c = 1$ corresponds to a fully inert particle. All reactive effects are neglected ($Da = 0$) and negative mobility $M = -1$ is considered, so the particles swim to the left. Bottom: Dependence on μ_c of the optimal Péclet number, Pe_M (dashed), leading to the maximum velocity, U_M (black solid), and of the self-propulsion velocity in the absence of advective effects, U_0 ($Pe = 0$, grey solid).

C. Optimal Pe for arbitrary Janus particles

The results in Fig. 11 suggest that the sensitivity to advective effects is strongly dependent on the extent of the reactive cap for an arbitrary Janus particle of negative mobility $M = -1$, and is non-symmetric with respect to $\mu_c = 0$. In particular, a maximum is reached for $\mu_c \approx -0.37$, with a sensitivity more than 25% greater than the sensitivity to Pe of the symmetric particle A ($\mu_c = 0$). The sensitivity to advective effects tends to vanish in the limit

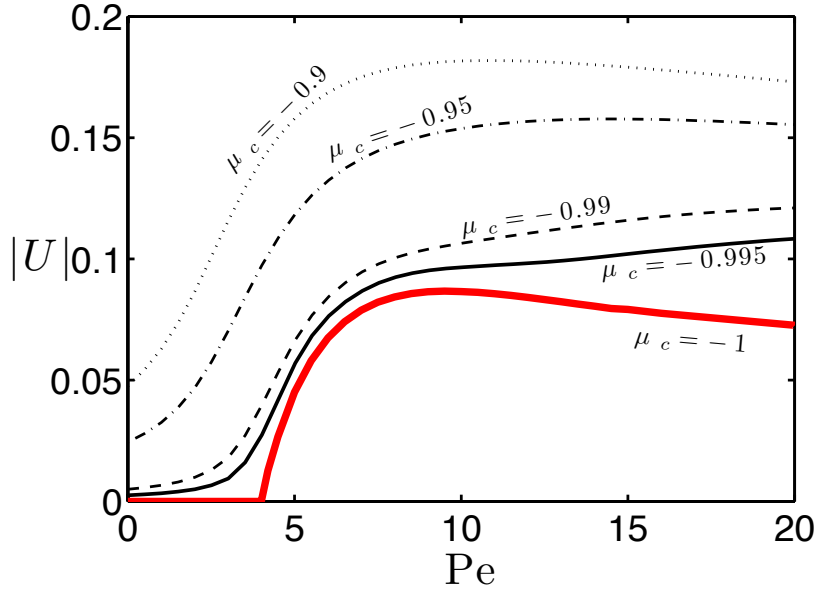


FIG. 13: (Colour online) Dependence of the velocity magnitude, $|U|$, with the Péclet number, Pe , of Janus particles with $\mu_c = -0.9$ (dotted line), $\mu_c = -0.95$ (dash-dotted), $\mu_c = -0.99$ (dashed), $\mu_c = -0.995$ (thin solid) with negative mobility. The velocity obtained for a strictly isotropic particle $\mu_c = 1$ and resulting from a symmetry-breaking instability [29] is shown in thick red line.

of isotropic inert or active particles ($\mu_c \rightarrow \pm 1$). Further, when comparing the sensitivity for two symmetric particles, i.e. those with inverse cap-size ratio or equivalently opposite μ_c , the most reactive particle is always more sensitive to advective effects. As $U \rightarrow 0$ when $Pe \rightarrow \infty$ for all Janus particles, these results demonstrate the existence of an optimal Pe for $M < 0$ leading to a maximum velocity.

This observation is confirmed using nonlinear numerical simulations and systematically varying μ_c and Pe . The results are shown in Fig. 12 where we display the iso-values of the phoretic velocity magnitude (top) and plot the value of the maximum swimming velocity and corresponding optimal Péclet number as a function of the active cap size, μ_c . Note that $Da = 0$ is chosen here since we identified a systematic penalization of the swimming velocity by reactive effects. The asymmetry between two symmetric particles P_1 and P_2 such that $k_{P_1}(\mu) = 1 - k_{P_2}(\mu)$ is apparent in Fig. 12. Advective effects are observed to significantly enhance the swimming velocity of particles with $\mu_c < 0$ (i.e. particles whose reactive cap is greater than the inert cap), while this effect is small for particles with smaller reactive caps ($\mu_c > 0$). This observation is consistent with a monotonic decrease with μ_c of the optimal Péclet number, Pe_M , at which the maximum velocity is achieved. A mostly inert particle will experience a small peak velocity for low Pe while mostly active particles experience a large velocity increase for $Pe \gtrsim 1-10$.

The limit $\mu_c \rightarrow -1$ is particularly intriguing. This corresponds to an almost fully-reactive particle except for a very small inert cap near the left pole. Such particles do not experience any significant self-propulsion at $Pe = 0$; however, Fig. 12 shows that such a particle may achieve a finite propulsion velocity for large Pe . Ref. [29] showed that the completely reactive particle ($\mu_c = -1$) may achieve self-propulsion at finite Pe despite spherical symmetry, through an instability and symmetry-breaking process arising from the nonlinear coupling of the solute dynamics and phoretic slip velocity near the surface of the particle. The mechanism leading to self propulsion at high Pe has the same origin. More precisely, the dependence of $|U|$ with Pe appears to converge asymptotically to that obtained for the isotropic reactive particle when $\mu_c \rightarrow -1$ (Figure 13). Infinitesimal velocities are obtained below the instability threshold $Pe = 4$ [see derivation in 29] and are solely due to the symmetry-breaking introduced by the presence of a small inert cap on the left. Beyond $Pe = 4$, the instability resulting from the nonlinear coupling of the surface phoretic flows and solute advection-diffusion dominates and leads to finite swimming velocity.

Finally, the dependence of the stresslet intensity, Σ , with Pe and μ_c also exhibits asymmetry, as shown in Fig. 14. At small Pe , the sign of μ_c determines the sign of the stresslet. In the case of negative mobility $M = -1$, mostly reactive particles behave as pullers ($\mu_c < 0$, $\Sigma > 0$) while mostly inert particles behave as pushers ($\mu_c > 0$, $\Sigma < 0$). The conclusions are reversed for $M = 1$. At intermediate and large Pe , this symmetry around $\mu_c = 0$ no longer holds and particles with a reactive cap slightly larger than a hemisphere may experience a change in the sign of their stresslet intensity becoming pushers at large Pe . For such particles, the maximum stresslet, resulting in the strongest

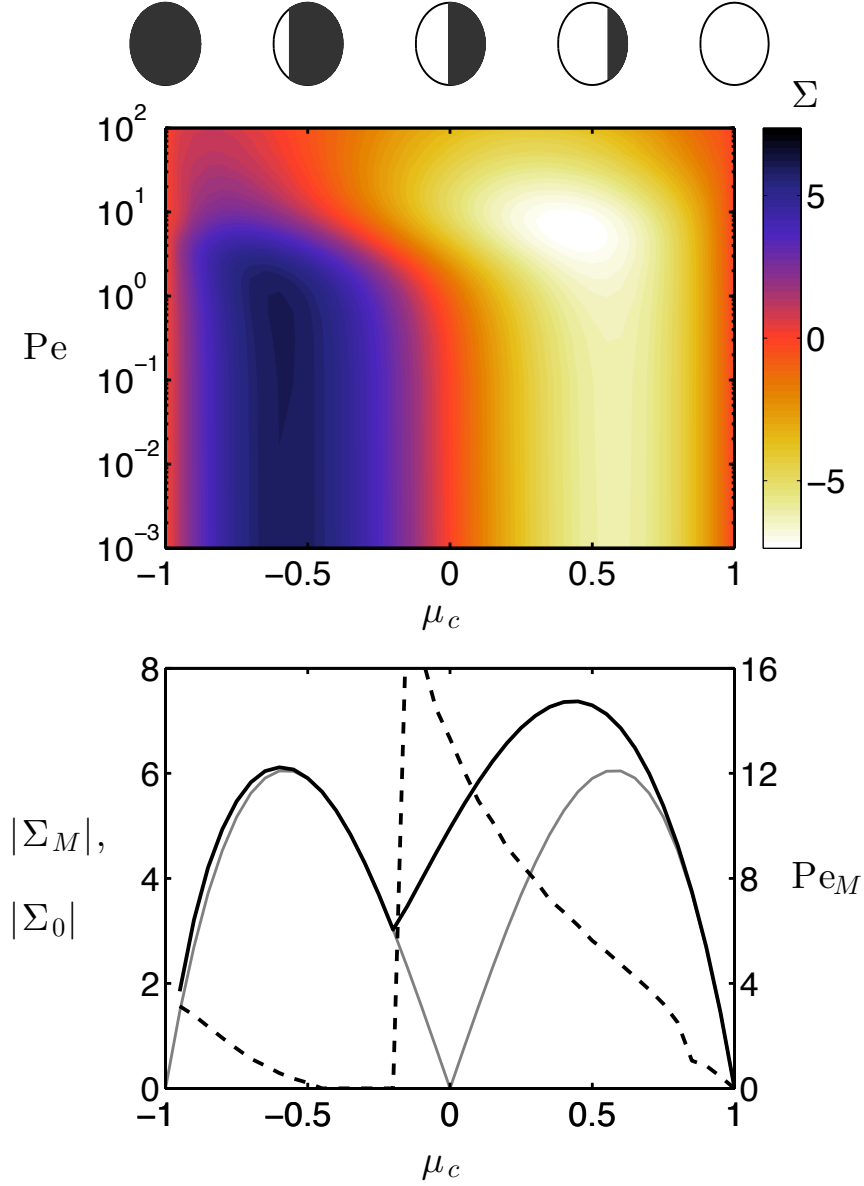


FIG. 14: (Colour online) Top: Dependence of the stresslet intensity, Σ , with Pe and the relative size of the reactive cap, μ_c . All reactive effects are neglected ($Da = 0$) and negative mobility $M = -1$ is considered (swimming occurs to the left). Bottom: Dependence on μ_c of the optimal Péclet number, Pe_M (dashed), leading to a maximum stresslet magnitude, $|\Sigma_M|$ (black solid), and of the stresslet magnitude in the absence of advective effects, $|\Sigma_0|$ ($Pe = 0$, grey solid).

inter-particle interaction, is obtained at large Pe . Results obtained for $M = 1$ (not shown here) exhibit the same dominance of the pusher characteristic: particles with $\mu_c > 0$, which are pullers at $Pe = 0$, become pushers at larger Pe .

VII. CONCLUSIONS

Our work generalizes the classical continuum phoretic framework to account for finite advective and reactive effects. Our results highlight the influence of such effects on the self-propulsion of axisymmetric Janus particles, and are relevant to phoretic particles of sufficiently large radius. In particular, advection of the solute by the phoretic flows can lead to significant increases in the swimming velocity, which may reach a maximum at a finite, order one value

of the Péclet number. When the surface chemistry corresponds to a solute consumption at the particle boundary, such a peak in the self-propulsion velocity is only observed for particles of negative mobility (corresponding to locally attractive solute-surface interactions), while particles of positive mobility experience a monotonic decrease of their propulsion velocity with Pe . The impact of the geometrical active vs. inert coverage of the particle surface was also identified. Particles that are predominantly reactive are more sensitive to advective effects and experience the largest increase in their swimming velocity at finite Pe , while such effects are almost negligible for predominantly inert particles.

In contrast, reactive effects always penalize the self-propulsion of Janus phoretic particles in all situations: when reaction acts too rapidly for the solute diffusion to refresh the solute content in the vicinity of the particle, the rate of consumption of the solute at the surface is reduced, effectively amounting to a reduction of surface activity that decreases the slip velocity and hence penalizes self-propulsion.

Notably, the situation in which we predict locomotion to be enhanced by advection effects (finite value of Pe) is that of the system recently considered in a number of experimental investigations [14, 15, 20]. In this setup, polymeric particles half coated with platinum are used to catalyze the autodegradation of hydrogen peroxyde, H_2O_2 , into dioxygen, O_2 . Self-diffusiophoresis due to the action of O_2 gradients corresponds to net locomotion with the polymeric side of the particle first: $k < 0$ and $M > 0$. This situation is equivalent to the case $k > 0$ and $M < 0$ computed above, and for which we predict locomotion to be enhanced by solute advection. Past experiments with this system have a Péclet number too small by about one order of magnitude for the effect to have been observed yet, but it could play a role in the case of larger particles. It also certainly plays an important role in the case of motion driven by surfactant gradients where, due to much smaller molecular diffusivity, Péclet numbers can easily reach $O(100)$ [42].

In this paper, we chose to focus exclusively on propulsion through self-diffusiophoresis of a particle, which catalyzes a simple one-step chemical reaction $S \rightarrow \emptyset$ on its surface. This framework can easily be extended to account for situations where both reagents and products of the reaction interact significantly with the surface or for multiple-steps reactions [e.g. see 14]. More generally, the results of our study are likely to remain valid for other phoretic mechanisms, provided the particle possesses two properties, namely *mobility* and *activity*. The former characterizes the ability of the particle to generate a slip velocity from an external field modified by advection and diffusion, while the latter corresponds to its ability to create local gradients of this field through chemical reaction or heat absorption/release [e.g. 5, 21].

Reactive and advective effects not only modify propulsion velocities but also significantly impact the flow field created by the particles and is therefore expected to modify the type and intensity of its hydrodynamic interactions with neighboring particles. The collective dynamics of such colloid particles was shown recently to exhibit different complex behaviours [32, 41]. A complete fundamental understanding of the mechanisms leading to such aggregations and collective organizations remains to be obtained. The results presented in this work however suggest that for larger particles, advective and, to a smaller extent, reactive effects may be significant.

Finally, the results obtained here rely on the assumption of a thin interaction layer, considered in most existing literature. We carefully identified the conditions under which this assumption and resulting framework are valid, namely when advection within the interaction layer can be neglected. The generalization of these results to the limit of very large Pe (i.e. when $\varepsilon Pe = O(1)$ or above) remains an open question. Depending on the nature of the solute-particle interaction, advection within the interaction layer may enhance or reduce the local solute gradients, respectively increasing or penalizing the self-propulsion velocity. Another interesting question to consider would be the effect of interactions between solute molecules, effectively introducing variations of the interaction potential with the solute concentration.

Appendix A: Generalization to non-uniform mobility

The framework and results presented in the main part of the paper can easily be extended to the case of a particle with non-uniform mobility which may be more relevant to experimental conditions. Indeed, the chemical treatment of the surface of the particle is likely to affect both surface activity and mobility. From a theoretical point of view, the phoretic problem formulation in Eqs. (44)–(48) remains valid for non-uniform $M(\mu)$. Its formulation in the squirmer framework is only marginally modified and while Eqs. (54)–(56) remain unchanged, Eq. (57) must be replaced by

$$\alpha_n = - \sum_{m,p=0}^{\infty} \frac{n(n+1)}{(2n+1)(2p+1)} M_p c_m(1) B_{mnp}, \quad (A1)$$

with B_{mnp} defined in Eq. (59) and $M(\mu) = \sum M_p L_p(\mu)$. We briefly show here that the results presented in the paper do remain valid when non-uniform mobility is considered, focusing on the configuration $M(\mu) = \pm k(\mu)$ (the chemical

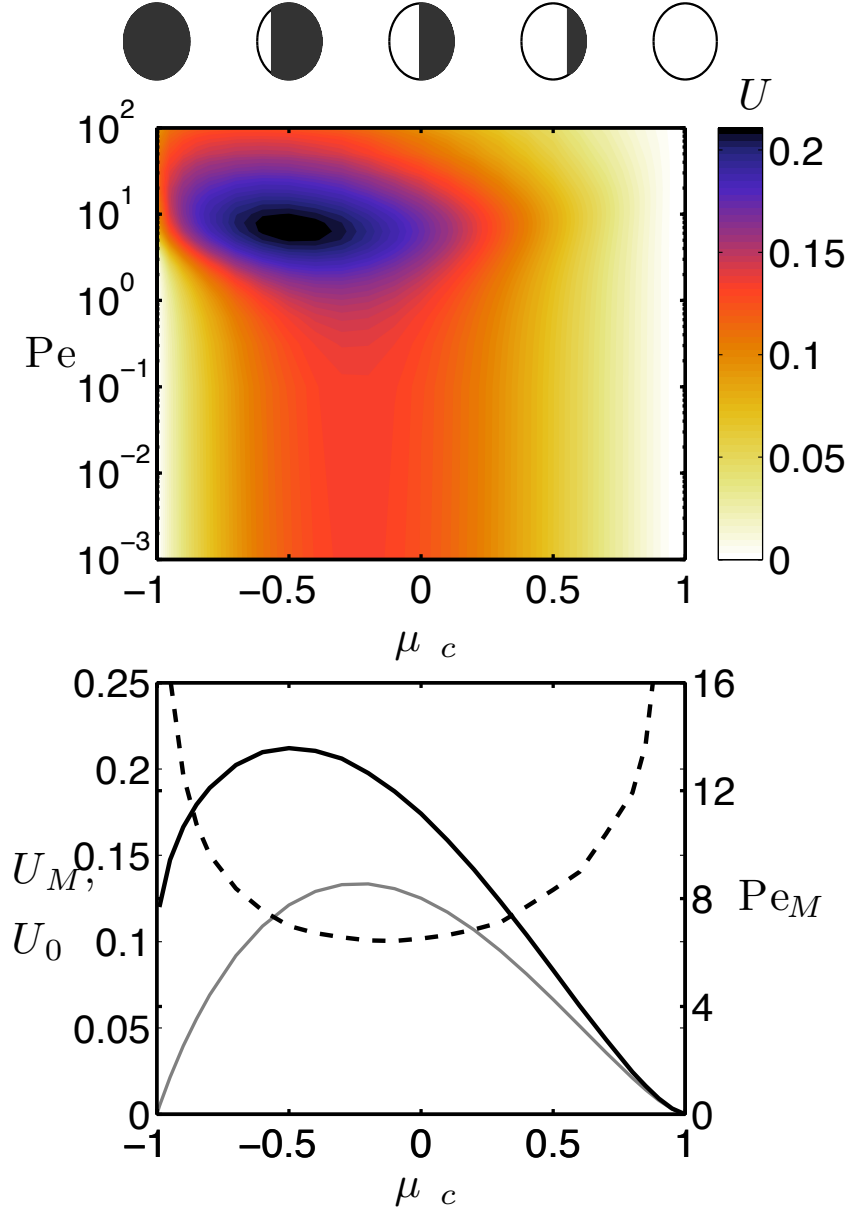


FIG. 15: Same results as Fig. 12 but for a particle with non-uniform mobility $M(\mu) = -k(\mu)$. Top: Dependence of the phoretic velocity magnitude with Pe and the relative size of the reactive cap, μ_c . Reactive effects are neglected ($Da = 0$) and negative mobility $M(\mu) = -k(\mu)$ is considered (swimming is thus to the left). Bottom: Dependence on μ_c of the optimal Péclet number, Pe_M (dashed), leading to the maximum velocity, U_M (black solid), and of the self-propulsion velocity in the absence of advective effects, U_0 ($Pe = 0$, grey solid).

patterning of the particle surface impacts both properties at the same time).

Figure 15 displays the dependence of the swimming velocity of the particle with Pe and the surface chemical coverage and generalize thus the results of Fig. 12 to the case of non-uniform mobility. The swimming velocity levels are generally obviously reduced since a smaller fraction of the particle contributes to the slip velocity, but the main conclusions of the paper are unchanged. Specifically, in the case of negative mobility, there exists an optimal $Pe(\mu_c)$ maximizing the swimming velocity. Further, this advective effect is more pronounced for particles whose reactive cap is greater than a hemisphere ($\mu_c < 0$). The analysis obtained for $\mu_c \rightarrow -1$ is also strictly equivalent to the uniform mobility case: in that limit, the existence of a small cap with zero mobility near the left pole does not modify the swimming velocity significantly since it corresponds to a small surface and the slip velocity in that region is almost

orthogonal to the swimming direction.

These results only differ from the ones in the main paper on two minor points. First the swimming velocity at $Pe = 0$ is no longer symmetric with respect to $\mu_c = 0$ and the optimal Pe for $\mu_c \rightarrow 1$ is large instead of converging to 0. The former result is a consequence of the greater surface contributing to the swimming velocity when $\mu_c < 0$ in comparison with $\mu_c > 0$. The latter indicates that the optimal velocity is reached for large Pe . However, as for the configuration with uniform mobility, this optimal velocity only marginally differs from the reference velocity U_0 and such Janus particles are still only weakly sensitive to advective effects. We finally note that for non-uniform mobility, advective effects can lead to stronger increases in the swimming velocity.

-
- [1] ANDERSON, J. L. 1989 Colloid transport by interfacial forces. *Ann. Rev. Fluid Mech.* **21**, 61–99.
 - [2] ANDERSON, J. L. & PRIEVE, D. C. 1991 Diffusiophoresis caused by gradients of strongly adsorbing solutes. *Langmuir* **7**, 403–406.
 - [3] BATCHELOR, G. K. 1970 The stress system in a suspension of force-free particles. *J. Fluid Mech.* **41**, 545–570.
 - [4] BENDER, C. M. & ORSZAG, S. A. 1978 *Advanced Mathematical Methods for Scientists and Engineers*. New York: McGraw-Hill.
 - [5] BICKEL, T., MAJEE, A. & WÜRGER, A. 2013 Flow pattern in the vicinity of self-propelling hot janus particles. *Phys. Rev. E* **88**, 012301.
 - [6] BLAKE, J. R. 1971 A spherical envelope approach to ciliary propulsion. *J. Fluid Mech.* **46**, 199–208.
 - [7] BRADY, J. 2011 Particle motion driven by solute gradients with application to autonomous motion: continuum and colloidal perspectives. *J. Fluid Mech.* **667**, 216–259.
 - [8] BRAY, D. 2000 *Cell Movements: From Molecules to Motility*. New York: Garland Science.
 - [9] BRENNEN, C. & WINNET, H. 1977 Fluid mechanics of propulsion by cilia and flagella. *Ann. Rev. Fluid Mech.* **9**, 339–398.
 - [10] BROYDEN, C. G. 1965 A class of methods for solving nonlinear simultaneous equations. *Math. Comp.* **19**, 577–593.
 - [11] CÓRDOVA-FIGUEROA, U. M. & BRADY, J. F. 2008 Osmotic Propulsion: The Osmotic Motor. *Phys. Rev. Lett.* **100** (15), 158303, see also the comments on this article by Jülicher & Prost, *Phys. Rev. Lett.*, **103**, 079801.
 - [12] CÓRDOVA-FIGUEROA, U. M., BRADY, J. F. & SHKLYAEV, S. 2013 Osmotic propulsion of colloidal particles via constant surface flux. *Soft Matter* **9**, 6382–6390.
 - [13] DREYFUS, R., BAUDRY, J., ROPER, M. L., FERMIGIER, M., STONE, H. A. & BIBETTE, J. 2005 Microscopic artificial swimmers. *Nature* **437**, 862–865.
 - [14] EBBENS, S., TU, M.-H., HOWSE, J. R. & GOLESTANIAN, R. 2012 Size dependence of the propulsion velocity for catalytic janus-sphere swimmers. *Phys. Rev. E* **85**, 020401.
 - [15] EBBENS, STEPHEN J. & HOWSE, JONATHAN R. 2011 Direct observation of the direction of motion for spherical catalytic swimmers. *Langmuir* **27**, 12293–12296.
 - [16] GAO, WEI, SATTAYASAMITSATHIT, SIRILAK, MANESH, KALAYIL MANIAN, WEIHS, DANIEL & WANG, JOSEPH 2010 Magnetically powered flexible metal nanowire motors. *J. Am. Chem. Soc.* **132**, 14403–14405.
 - [17] GHOSH, A. & FISCHER, P. 2009 Controlled propulsion of artificial magnetic nanostructured propellers. *Nano Lett.* **9**, 2243–2245.
 - [18] GOLESTANIAN, R., LIVERPOOL, T. B. & AJDARI, A. 2005 Propulsion of a molecular machine by asymmetric distribution of reaction products. *Phys. Rev. Lett.* **94** (22), 220801.
 - [19] GOLESTANIAN, R., LIVERPOOL, T. B. & AJDARI, A. 2007 Designing phoretic micro- and nano-swimmers. *New J. Phys.* **9**, 126.
 - [20] HOWSE, JONATHAN R., JONES, RICHARD A. L., RYAN, ANTHONY J., GOUGH, TIM, VAFABAKHSH, REZA & GOLESTANIAN, RAMIN 2007 Self-motile colloidal particles: From directed propulsion to random walk. *Phys. Rev. Lett.* **99**, 048102.
 - [21] JIANG, H.-R., YOSHINAGA, N. & SANO, M. 2010 Active motion of a Janus particle by self-thermophoresis in a defocused laser beam. *Phys. Rev. Lett.* **105**, 268302.
 - [22] JÜLICHER, F. & PROST, J. 2009 Comment on “Osmotic propulsion: the osmotic motor”. *Phys. Rev. Lett.* **103**, 079801.
 - [23] JÜLICHER, F. & PROST, J. 2009 Generic theory of colloidal transport. *Eur. Phys. J. E* **29** (1), 27–36.
 - [24] KHAIR, A. S. 2013 Diffusiophoresis of colloidal particles in neutral solute gradients at finite Péclet number. *J. Fluid Mech.* **731**, 64–94.
 - [25] LAUGA, E. & POWERS, T. R. 2009 The hydrodynamics of swimming micro-organisms. *Rep. Prog. Phys.* **72**, 096601.
 - [26] MAGAR, V., GOTO, T. & PEDLEY, T. J. 2003 Nutrient uptake by a self-propelled steady squirmer. *Q. J. Appl. Maths* **56**, 65–91.
 - [27] MICHELIN, S. & LAUGA, E. 2011 Optimal feeding is optimal swimming for all Péclet numbers. *Phys. Fluids* **23** (10), 101901.
 - [28] MICHELIN, S. & LAUGA, E. 2013 Unsteady feeding and optimal strokes of model ciliates. *J. Fluid Mech.* **715**, 1–31.
 - [29] MICHELIN, S., LAUGA, E. & BARTOLO, D. 2013 Spontaneous autophoretic motion of isotropic particles. *Phys. Fluids* **25**, 061701.
 - [30] NELSON, BRADLEY J., KALIAKATSOS, IOANNIS K. & ABBOTT, JAKE J. 2010 Microrobots for minimally invasive medicine. *Annu. Rev. Biomed. Eng.* **12** (1), 55–85.
 - [31] O’BRIEN, R. W. 1983 The solution of the electrokinetic equations for colloidal particles with thin double layers. *J. Colloid*

Interface Sci. **92**, 204–216.

- [32] PALACCI, J., SACANNA, S., STEINBERG, A. P., PINE, D. J. & CHAIKIN, P. M. 2013 Living crystals of light-activated colloidal surfers. *Science* **339**, 936–940.
- [33] PAXTON, W F, KISTLER, K C, OLMEDA, C C, SEN, A, ANGELO, S K St, CAO, Y, MALLOUK, T E, LAMMERT, P E & CRESPI, V H 2004 Catalytic Nanomotors: Autonomous Movement of Striped Nanorods. *J. Am. Chem. Soc.* **126** (41), 13424–13431.
- [34] POPESCU, M. N., DIETRICH, S., TASINKEVYCH, M. & RALSTON, J. 2010 Phoretic motion of spheroidal particles due to self-generated solute gradients. *Eur. Phys J. E* **31**, 351–367.
- [35] PRIEVE, D. C., ANDERSON, J. L., EBEL, J. P. & LOWELL, M. E. 1984 Motion of a particle generated by chemical gradients. part 2. electrolytes. *J. Fluid Mech.* **148**, 247–269.
- [36] PURCELL, E. M. 1977 Life at low Reynolds number. *Am. J. Phys.* **45**, 3–11.
- [37] SABASS, B. & SEIFERT, U. 2012 Dynamics and efficiency of a self-propelled, diffusiophoretic swimmer. *J. Chem. Phys.* **136**, 064508.
- [38] SCHMITT, M. & STARK, H. 2013 Swimming active droplet: a theoretical analysis. *Eur. Phys. Lett.* **101**, 44008.
- [39] SHARIFI-MOOD, N., KOPLIK, J. & MALDARELLI, C. 2013 Diffusiophoretic self-propulsion of colloids driven by a surface reaction: the sub-micron particle regime for exponential and van der Waals interactions. *Phys. Fluids* **25**, 012001.
- [40] STONE, H. A. & SAMUEL, A. D. T. 1996 Propulsion of microorganisms by surface distortions. *Phys. Rev. Lett.* **77**, 4102.
- [41] THEURKAUFF, I., COTTIN-BIZONNE, C., PALACCI, J., YBERT, C. & BOCQUET, L. 2012 Dynamic clustering in active colloidal suspensions with chemical signaling. *Phys. Rev. Lett.* **108**, 268303.
- [42] THUTUPALLI, S., SEEMANN, R. & HERMINGHAUS, S. 2011 Swarming behavior of simple model squirmers. *New J. Phys.* **13**, 073021.
- [43] WALTHER, A. & MÜLLER, A. H. E. 2008 Janus particles. *Soft Matter* **4**, 663–668.
- [44] WANG, JOSEPH 2009 Can man-made nanomachines compete with nature biomotors? *ACS Nano* **3**, 4–9.
- [45] YARIV, E. 2010 An asymptotic derivation of the thin-Debye-layer limit for electrokinetic phenomena. *Chem. Eng. Comm.* **197**, 3–17.
- [46] YOSHINAGA, N., NAGAI, K. H., SUMINO, Y. & KITAHATA, H. 2012 Drift instability in the motion of a fluid droplet with a chemically reactive surface driven by marangoni flow. *Phys. Rev. E* **86**, 016108.
- [47] ZHANG, LI, PEYER, KATHRIN E. & NELSON, BRADLEY J. 2010 Artificial bacterial flagella for micromanipulation. *Lab Chip* **10**, 2203–2215.